이학박사 학위논문

Electrical Characteristics of Organic Semiconductor and Molecular Junctions in Vertical Structure with Graphene Electrode

그래핀 전극 기반 수직구조 형태의 유기·분자 접합의 전기적 특성에 대한 연구

2020 년 8 월

서울대학교 대학원

물리·천문학부

황 왕 택

Electrical Characteristics of Organic Semiconductor and Molecular Junctions in Vertical Structure with Graphene Electrode

그래핀 전극 기반 수직구조 형태의 유기·분자 접합의 전기적 특성에 대한 연구

지도교수 이 탁 희

이 논문을 이학박사 학위논문으로 제출함

2020 년 7 월

서울대학교 대학원

물리천문학부

황 왕 택

황왕택의 이학박사 학위논문을 인준함

2020 년 6 월

위 원 장 _____ 이 진 호 (인)

부위원장 _____ 이 탁 희 (인)

위 원 _____ 김 기 훈 (인)

위 원 _____ 박 윤 (인)

위 원 _____ 왕 건 욱 (인)

Abstract

Electrical Characteristics of Organic Semiconductor and Molecular Junctions in Vertical Structure with Graphene Electrode

Wang-Taek Hwang
Department of Physics and Astronomy
Seoul National University

Molecular electronics has been studied for a few decades to understand the charge transport characteristics through the molecular wires and use molecules as components of the electronic devices. Molecular electronic devices that function as resistor, diode, memory, or transistor have been demonstrated in various device platforms by taking advantages of the molecular electronics such as low cost and high throughput, synthetic variability of functional molecules, and self-assembly. However, researches on the single molecule junctions functioning as the field-effect transistor (FET) which is the most important basic element that makes up logic circuits in modern electronics has limitation to practical device applications. In this regard, I studied the field-effect molecular electronic device in a large area junction platform to exploit its advantage of high device yield and mass production.

The first topic of my study is the fabrication and characterization of the pentacene barristor. The pentacene barristor has a device structure and transport mechanism

similar to the molecular field-effect device but can be fabricated in an easier method. I studied the electrical properties of the pentacene barristor which showed the asymmetric characteristics with the bias- and the gate-voltage dependences. Temperature-variable measurement was carried out and it was demonstrated that the charge transport mechanism of this device was either thermionic emission and the Poole-Frenkel conduction based on the applied bias.

The next topic is the fabrication of alkanethiol junctions with inverted self-assembled monolayer (SAM) which is an alternative fabrication method for the large area molecular junctions. In contrast to the general molecular ensemble junctions in which SAM is deposited on the bottom electrodes, the top electrode with pre-deposited SAM was transferred onto the bottom electrode in the inverted SAM junction. I demonstrated Au-molecule-Au junctions with the reference molecules (alkanethiols) and compared the electrical properties with the molecular junctions with alkanethiols in various testbeds.

Finally, rectifying molecules under the gate electric field is studied. Ferrocenyl alkanethiol molecule was employed to exhibit the diode-like property and the ionic gel was applied as the top-gate dielectric giving a strong field-effect. This molecular device showed the rectification modulated by bias- and gate-voltages.

Keywords: Molecular electronics, Graphene, Self-assembled monolayer, Pentacene, Barristor, Alkanethiol, Charge transport

Student Number: 2013-20388

List of Contents

List of Figures and Tables

Figure 1.9 Electrical characteristics of PALO junctions. (a) Semi-log plot of the tunneling conductivity versus chain-length of fatty acid monolayers. The fit to a straight line gives a slope of β = 0.86 Å^{-1}. (b) Temporal plot of the remnant current (circles) as a function of applied bias (crosses), displaying switching behavior upon reaching a threshold voltage: 1 V for turning "on" and –0.6 V for turning "off".

Figure 1.10 Electrical characteristics of DMT junctions. (a) Statistical *J–V* data for C8, C12, and C16 working devices. (b) Distribution of the logarithmic current densities at 1 V for all molecular junctions. (c) A semi-log plot of the current densities measured at different biases as a function of the molecular length. Solid lines represent the exponential fitting results, in which the slope is related to the decay coefficient β. The inset shows the values of β deduced from the plot versus the applied bias. (d) Arrhenius plot of the logarithmic current densities for C8, C12 and C16 molecular junctions at different biases from 0.2 V to 1.0 V in 0.2 V increments. The temperature was varied from 80 K to 295 K in 40 K increments. (e) IETS data of six C12 molecular junctions measured at 4.2 K. Each arrow indicates the corresponding molecular vibration modes of the C12 molecule. Peaks that cannot be assigned to any possible vibrational modes of the molecule are marked with asterisks. In this plot, shaded squares are used to compare each characteristic peak from device to device.

Figure 1.11 Schematic illustration of the device fabrication process for the graphene electrode molecular junctions.

Figure 1.12 Statistical *J-V* data for all (a) C8, C12, C16 and DC8 molecular junctions (Reproduced with permission from ref 25. Copyright 2010 John Wiley & Sons), (b) BDT, BPDT, TPDT molecular junctions. (c) A semi-log plot of the *J* values at different biases versus the numbers of phenyl rings in the BDT, BPDT, and TPDT molecular junctions. (d) Current densities measured at 0.8 V in different bending configurations (bending radii of ∞, 10 mm, and 5 mm). (e) d^2I/dV^2 plot of a BDT molecular junction with a graphene electrode. In the d^2I/dV^2 plot, IETS peaks can be observed at 21, 82, 136, and 209 mV.

Figure 3.4 Plot of ln(J) as a function for the number of carbons at different bias voltages. The values of decay coefficient β (~1.17 per carbon) are extracted from the slopes of the exponentially fitted lines (solid lines).

Table 3.1 The summary of the statistical analysis.

Chapter 1. Introduction

1.1. Overview of Molecular Electronics

In the past decades, the modern electronics based on the semiconductor has made remarkable progress in terms of integration and miniaturization of the electrical circuits and it leads the modern technology and industry. As the development of the silicon-based electronics represented by the Moore's law, however, has been slow down in the scale of a few nanometer due to the quantum interference, tunneling effect or heat dissipation, several candidates emerged to overcome such limitation.

Molecular electronics is one of the fascinating candidates with determinant advantages. Because the molecules are employed as the building-block of the electric components, the functionality of the molecular electronic devices can be controlled by synthesizing the molecules with infinite degrees of freedom. Construction of nanostructures by the bottom-up process is also possible because of the self-assembling nature of the molecules with special anchoring groups.

Since the theoretical study by Aviram and Ratner in 1974[1], the molecular electronics has drawn a great interest because single-molecules or molecular layers can be utilized as electronic transport channels. The major goal in this research field is understanding of intrinsic properties of the molecules. At the same time the experiment techniques including molecular synthesis, device fabrication, measurement and analysis have also been important topics in molecular electronics. Fabrication of molecular junctions is still a challenging issue because it is difficult

to connect the small molecules in length scale of ~1 nm to the electrical leads for electrical measurements.

1.2. Brief Introduction of Theoretical Background

1.2.1. Landauer formalism

In the mesoscopic systems in which the wave nature of the electrons dominates charge transport, there are limitations of the (semi)classical approaches to account for the electrical properties in this system. The quantum mechanical approach shown by R. Landauer[2] in 1950's determines the total conductance G in the nanoscale devices by the Landauer formula,

$$G = \frac{2e^2}{h}\sum_{n=1}^{N} T_n \qquad \text{Eq. 1.1}$$

where e is the elemental charge, h is the Planck's constant, and T_n's are the transmissions of all available conduction channels in the junction. In other words, the conductance is the summation of the transmission of the current-carrying eigenmodes.

The typical nanoscale devices consist of two electrodes and channel material in which the charge carriers are scattered. The total current that flows from left electrode to right is deviated from the quantum mechanical expression of the current density with the scattering approach as the integration of the transmission in the bias window.

$$I = \frac{2e}{h}\int_{-\infty}^{\infty} dE\, T(E)\,[f_L(E) - f_R(E)] \qquad \text{Eq. 1.2}$$

where f_L and f_R is the Fermi distributions of the electrodes on the left (L) or right (R) of the scattering centers (or the potential barriers).

In the most molecular junctions, the frontier orbital (the closest molecular orbital level to the Fermi of electrode) is considered as dominating the charge transport. In that case, the charge transports between this orbital and electrodes are analogous to the double barrier tunneling illustrated in Figure 1.1.

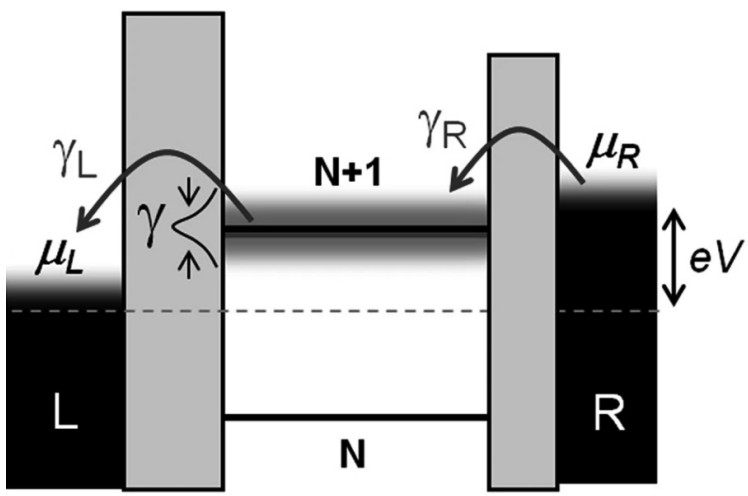

Figure 1.2 Schematics of the electrical coupling in a molecular junction with multiple orbital levels sandwiched between two leads (L (left), R (right)). The parameters determining transport are the coupling (or tunneling rate) $\gamma_{\frac{L}{R}}$, the electrostatic potentials of leads $\mu_{\frac{L}{R}}$, and energy level broadening $\gamma = \gamma_L + \gamma_R$ [Garrigues et al., *Scientific Reports*, 6, 26517 (2016)]

The transmission $T(E)$ in the double barrier tunneling model is expressed as the Lorentzian distribution

$$T(E) = \frac{4\gamma_L\gamma_R}{(E-\varepsilon_0)^2 + (\gamma_L+\gamma_R)^2} \qquad \text{Eq. 1.3}$$

where $\gamma_{\frac{L}{R}}$ are the scattering rates of each barriers and ε_0 is the resonant energy level.

Charge transport at the interface between lead and molecule can be considered as a tunneling process. As the strength of the coupling increases, tunneling rates are also enhanced. The broadening of molecular level also occurs due to the hybridization with the metallic states and the half-width at half-maximum (HWHM) is given by $\gamma = \gamma_L + \gamma_R$. When the molecular level ε_0 lies at the Fermi level of electrodes, the resonant tunneling occurs.

Although the Landauer formalism explains basic transport in the mesoscopic systems including the molecular junctions very successfully, this scattering approach is not valid when the inelastic scattering cannot be neglected. One must also assume the phase-coherent transport over the entire sample. In reality, these conditions are valid at zero temperature and for electrons at the Fermi level[3].

1.2.2. Simmons model

The charge transport in the most molecular junctions can be simplified as the transmission through a potential with various shapes depending on the bias voltage. The formula that Simmons derived in 1963[4] is simple but powerful tool to analyze the current-voltage (I-V) characteristics of the metal-insulator-metal junctions with

a barrier of arbitrary shape including molecular junctions.

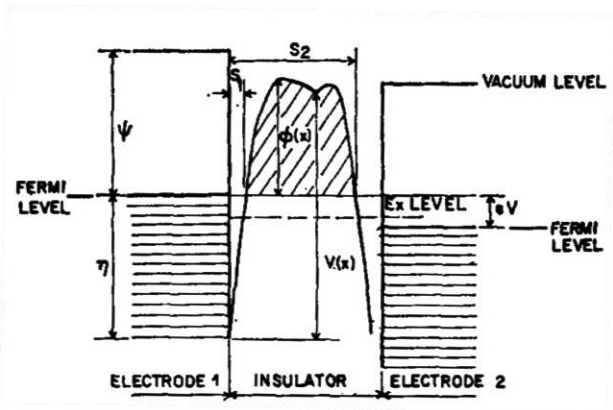

Figure 1.2 Schematics of metal-insulator-metal (MIM) structure with an arbitrary potential barrier

Simmons model was derived with the help of WKB approximation to calculate the transmission $T(E)$ of the junction. The general form of this formula is

$$J = J_0\{\varphi_B \exp(-A\sqrt{\varphi_B}) - (\varphi_B + eV)\exp(-A\sqrt{\varphi_B + eV})\}, \qquad \text{Eq. 1.4}$$

where φ_B is the average barrier height at zero bias relative to the reference electrode and,

$$A = \frac{2\alpha d}{\hbar}\sqrt{2m} \text{ and } J_0 = \frac{e}{2\pi h \alpha^2 d^2} \qquad \text{Eq. 1.5}$$

where $\hbar = \frac{h}{2\pi}$, α is a correction factor, d is the barrier width and m is the mass of electron.

In the low bias region ($eV \sim 0$), this equation is reduced to the form of

$$J \propto \frac{V}{d}\exp\left(-\frac{2\alpha d}{\hbar}\sqrt{2m\varphi_B}\right) \qquad \text{Eq. 1.6}$$

, which describes the direct tunneling. I-V characteristics in the high bias region ($eV > \varphi_B$) is simplified into

$$J \propto V^2 \exp\left(-\frac{4\alpha d\sqrt{2m}\varphi_B^{3/2}}{3e\hbar V}\right) \quad \text{Eq. 1.7}$$

, which describes the Fowler-Nordheim tunneling or field emission. One can estimate the barrier height of a molecular junction by finding the transition voltage at which the characteristic behavior changes between the direct tunneling and field emission.

Notice that these two tunneling conductions deviated from the Simmons model are independent on the temperature.

1.2.3. Temperature-dependent conductions

In addition to the tunneling process, there are another conduction mechanisms that describe charge transport across the barrier. Thermionic emission is the excitation of electrons over a potential barrier by thermal energy. The temperature dependency of this conduction is very strong and significant in the condition of low potential barrier. Remarkably, the energy and phase are preserved during this process so this is one of the coherent transports. The temperature- and voltage- dependence are described as

$$\ln\left(\frac{J}{V^2}\right) \sim \frac{1}{T} \quad \text{and} \quad \ln J \sim V^{\frac{1}{2}} \quad \text{Eq. 1.8}$$

Another thermally activated transport mechanism is the hopping conduction in which the electrons move by hopping the point at which the wave functions of electron are localized within the molecule. It was reported that this conduction is dominant the transport in the long conjugated molecule[5]. The I-V and I-T characteristics of this conduction are known as

$$\ln\left(\frac{J}{V}\right) \sim \frac{1}{T} \quad \text{and} \quad J \sim V \qquad \text{Eq. 1.9}$$

The Poole-Frenkel effect explains the conduction in an electrical insulator with trap sites. The electrons are trapped in the localized states, then de-trapped and moved to the conduction band by the thermal energy. In the case of the presence of the large electric field, the effective depth of trap sites is reduced and the electrons are able to escape the trap with less thermal energy. The electrical characteristic is expressed as

$$J \propto F \exp\left(-e\frac{\varphi_T - \sqrt{eF/\pi\varepsilon}}{kT}\right) \qquad \text{Eq. 1.10}$$

where F is the applied electric field, φ_T is the potential depth of trap, ε is the dynamic permittivity and k is the Boltzmann's constant.

1.3. Experimental Testbed in Molecular Electronics

1.3.1. Self-assembled monolayer

Self-assembly has been a useful strategy to deposit the molecules onto the surface of metal electrodes. This bottom-up fabrication technology can be conducted in gas or liquid environments, and the latter is more popular method featuring its accessibility and simplicity. As the formation of self-assembled monolayer (SAM) is the most important process to decide the quality of the molecular junctions, various investigations have been carried out to understand the fundamental mechanisms that drive this step. The reference system focused on is the adsorption of the alkanethiolates on the Au(111) surface.

The initial step of the SAM formation is believed as highly disordered system physisorbed on Au(111). After physisorption, the thiol anchoring groups chemisorb on the Au(111) face through the sulfur headgroup and form strong covalent bond and form lying down phase. The adsorption process can be written as follows

$$RS\text{-}H + Au \rightarrow RS\text{-}Au + 0.5\ H_2 \qquad \text{Eq. 1.11}$$

Since the chemisorption of the thiol molecules is easier at the defect sited of the Au surface, where the nucleation of standing up phase starts. These islands grows and the surface coverage of SAM increase. These processes during formation of SAM are illustrated in Figure 1.3[6].

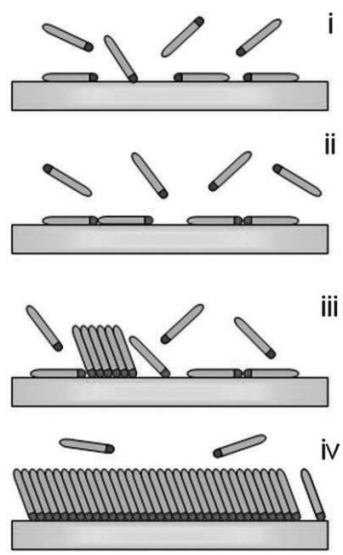

Figure 1.3 Scheme of the different steps taking place during the self-assembly of alkanethiol on Au(111): (i) physisorption, (ii) lying down phase formation, (iii) nucleation of the standing up phase, (iv) completion of the standing up phase[6]

1.3.2. General testbeds for molecular junctions

Single-molecular junctions are a traditional platform to study the electronic transport in molecular wire. Scanning tunneling microscope[7,8] (STM) conducting probe atomic force microscope[9] (C-AFM) are widely used tools that build the molecular junctions by contacting their tips to the molecular layer deposited on the specific surfaces. Another way to fabricate the single-molecular junction is to insert the molecule into a nano-gap of broken wire. Electro-migration break junction[10–12] and mechanically controllable break junction [13,14] (MCBJ) are representative methods to create nano-gap in the wire.

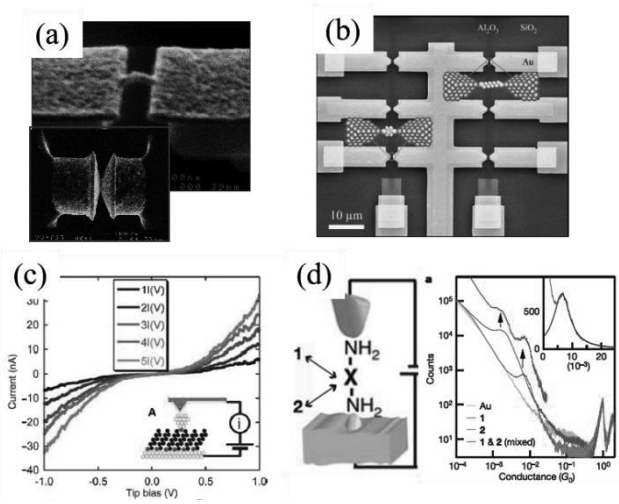

Figure 1.4 Examples of single-molecule junctions. (a) Mechanically controllable break junction[13], (b) Electro-migration break junction[11], (c) Conducting probe atomic force microscope[9], (d) Scanning tunneling microscope[15].

Another testbed for the experiment in molecular electronics is large-area ensemble molecular junction in which many molecules (> ~1000 molecules) exist in the junction and are involved in the charge transport. Typical structure of these junctions

is a vertical stack of 'bottom electrode – molecular layer – top electrode'. Molecular monolayer can be deposited on the surface of bottom electrode by using the self-assembly nature of molecules with certain end groups, so such molecular layer is called self-assembled monolayer (SAM). For example, thiol (-SH) moiety of a molecule makes covalent bonds with Au, Ag, or Pt surfaces[16]. Langmuir-Blodgett (LB) film[17,18] is also used for preparing homogeneous molecular layer by utilizing the surfactant molecules arranging at air-solvent interface.

Forming the top electrode on the molecular layer is the major challenge in building the large-area molecular junctions. The simplest way for that is direct deposition using thermal or electron-beam evaporator, but this method makes most junctions electrically shorted because metal filaments are grown through the thin molecular layer[19,20]. To enhance the junction yield, buffer interlayer-based junction[21–23] or liquid metal contact[24–26] were introduced.

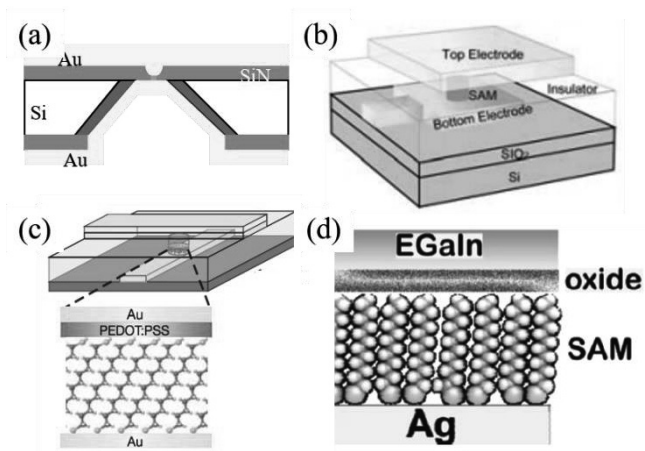

Figure 1.5 Schemes of large-area molecular junctions. (a) Nanopore[27], (b) Microscale via-hole[28], (c) Conducting polymer[21], (d) Eutectic GaIn contact junction[29].

Several studies about large-area molecular junctions fabricated by 'electrode-transfer'[30–37] have been reported, in which pre-made electrodes on the dummy substrate are transferred on the molecular layer. Since the transferred electrodes contact with molecular layer without metal filaments, this is an alternative fabrication method for molecular junctions that do not damage the molecular layer and secures high device yield. In the next section, I review the molecular electronic junctions with the transferred top electrodes in terms of materials for the electrodes (e.g. Au and graphene) and summarize their fabrication processes, electrical properties, and application for the functional molecular junctions.

1.3.3. Molecular junctions with transferred gold electrode

(a) Overview

Nanopore or *via*-hole technique[38,39] are traditional method fabricating the large-area ensemble molecular junctions in which the top metal contact is created by direct vacuum evaporation. They are suitable for investigation about the intrinsic transport in molecular wire because pure metal-molecule-metal junctions are ensured but applying them to the practical devices is difficult due to their low device yield (~ 1 %). Employing conducting polymer as buffer interlayer[21–23] or liquid metal contact of eutectic GaIn [24–26] makes a huge improvement in device yield but ambiguity at molecule-interlayer has been remained. Therefore, gold electrode-transfer is suitable testbed to study the transport across molecule-metal interface while satisfying moderate device yield for practical application. Several kinds of the molecular junctions by gold electrode-transfer has been reported. Their device

fabrication processes and schematics are summarized in Figure 1.6 and the detailed explanations for each junction are in following sections.

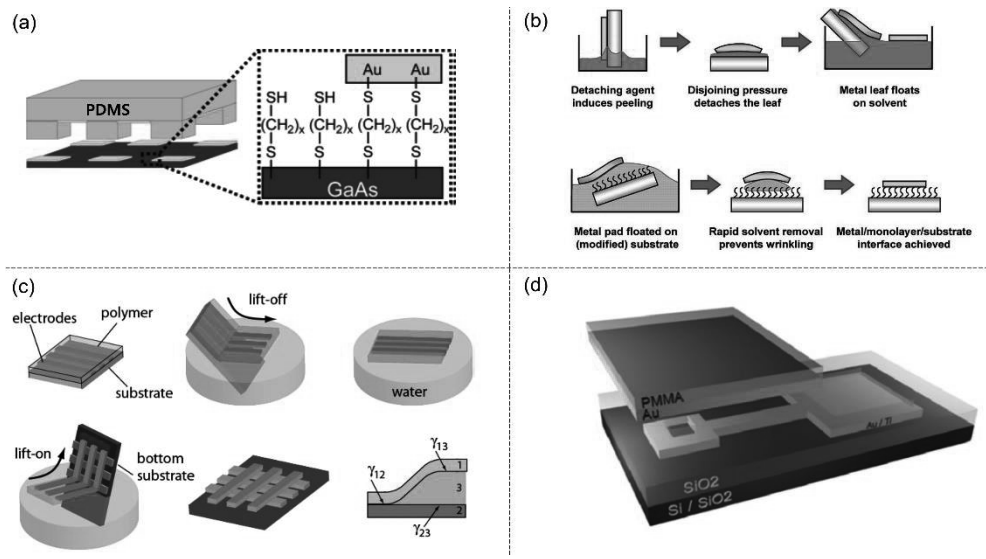

Figure 1.6 Schematics for fabrication procedure of large-area molecular junctions by (a) nanotransfer printing (nTP) [30], (b) lift-off float-on (LOFO) [40] (c) polymer-assisted lift-off (PALO) [32], and (d) direct metal transfer (DMT) [33].

(b) Nano-transfer printing

Figure 1.6(a) illustrates the molecular junction fabricated in nano-transfer printing (nTP) technology introduced by Loo *et al*. [30] It is obtained by transferring the metal film onto the molecule-treated substrate from the elastomeric poly-(dimethylsiloxane) (PDMS) stamp. In this work, GaAs / SAM / Au junctions are fabricated with various junction area and their electric characteristics are shown in

comparisons with junctions fabricated by direct metal evaporation method to provide insight into how top metal film fabrication affects the electrical transport in molecular electronic junctions.

To fabricate nTP molecular junctions, the conductive n^+ GaAs substrate is prepared for the bottom electrode of the junctions. After chemical etching the surface to remove native oxide, the substrate is immediately exposed to saturated molecular vapor of octanedithiol (DC8) in a desiccator. Only one end of molecules reacts with the GaAs surface and monolayer of DC8 is self-assembled on the surface. Then a fresh gold-coated PDMS stamp is brought into contact with the SAM-treated GaAs substrate without applying additional pressure. To release the Au pattern from the stamp, the surface chemistry must be considered. The spontaneous chemical bonding of S – Au at the SAM / Au interface facilitates the pattern transfer. In addition to providing strong adhesion between Au pattern and GaAs substrate, DC8 molecular layer serves as the electrical component in these molecular junctions.

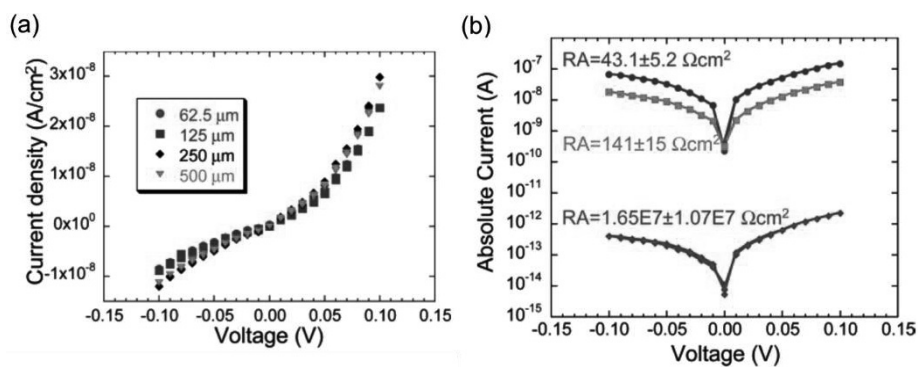

Figure 1.7 Electrical characteristics of nTP junctions (a) Current density as a function of applied voltage. (b) Absolute current levels (on a log scale) for applied voltage; Control sample (blue circles). Evaporated sample (green squares). nTP samples (red diamonds) [30]

The current-voltage (*I-V*) measurement for nTP molecular junction with different contact areas (circular Au patterns with diameters of 62.5, 125, 250, and 500 μm) were performed and the results are depicted in Figure 1.7(a). The scaling of total current with contact area shows the uniform current distribution in nTP junctions. The specific resistances (RA, R is the slope in the small bias region of the *I-V* curve, A is the contact area) for almost devices are also distributed within an order of magnitude. These results show that nTP is an effective fabrication method for reliable and reproducible molecular electronic devices.

Figure 1.7(b) shows *I-V* curves for the control (GaAs / Au junction), evaporated and nTP junctions with the same contact area. The effective barrier heights in each junction can be obtained by analyzing the electrical characteristics with the thermionic emission model. The extracted effective barrier heights of the control and evaporated junctions are 0.55 and 0.58 V which are lower values than the Schottky barrier height at n^+ GaAs / Au interface (0.7 V). These results indicate the generation of the ohmic contact, which are consistent with the large current densities for the control and evaporated junctions. However, the higher effective barrier height (~ 0.9 V) extracted from the *I-V* curve of nTP junction implies that the ohmic fraction are not present, thus tunneling through the molecular layer can be major transport channel in these junctions. The transport through ohmic contact in the evaporation sample and the tunneling through SAM in the nTP sample make the deviation of effective barrier heights from the ideal Schottky contact in opposite direction.

Although this early work for nTP junction introduced the platform of mass production of high-yield molecular devices with various junction area and which

enabled the statistical analysis, one challenge was the rough surface of top electrode generated during metal evaporation on the PDMS stamp. Roughness of electrode may generate small vacancies at SAM / metal electrode, which lead unreliable electrical properties.

(c) Lift-off and float-on approach

Thin metal films floating on the surface of liquid would be applied as the top electrode of molecular junctions. Figure 1.6(b) illustrates the device fabrication procedure based on such idea, termed as 'lift-off, float on (LOFO)', developed by Cahen *et al.* [40] Metal film deposited on the clean glass slide detached by etching solution then the 'metal leaf' leaves to float on the solvent with proper surface tension (upper part in Figure 1.6(b)). Molecular treated substrate is lifted with the leaf on top and the vertical structure of metal / molecule / substrate is made with the help of capillary interaction during drying the common liquid (lower part in Figure 1.6(b)). Comprehensive study for generating the LOFO junctions was also reported, [41] which accounts for the major forces related to the process. This work introduces the major challenges and provides solutions in qualitative manner.

Several kinds of molecular junctions with different semiconductor substrates such as GaAs [31], Si [42], and ZnO [43] were investigated. In these studies, the effects of molecular dipole at metal / semiconductor interface for electrical characteristics were discussed. Figure 1.8 shows the different *I-V* curves in the GaAs / molecule / Au junctions fabricated in LOFO method.[31] By using the nature dicarboxylic acid group that bonding to GaAs, molecular monolayers of tartaric acid derivatives (inset of

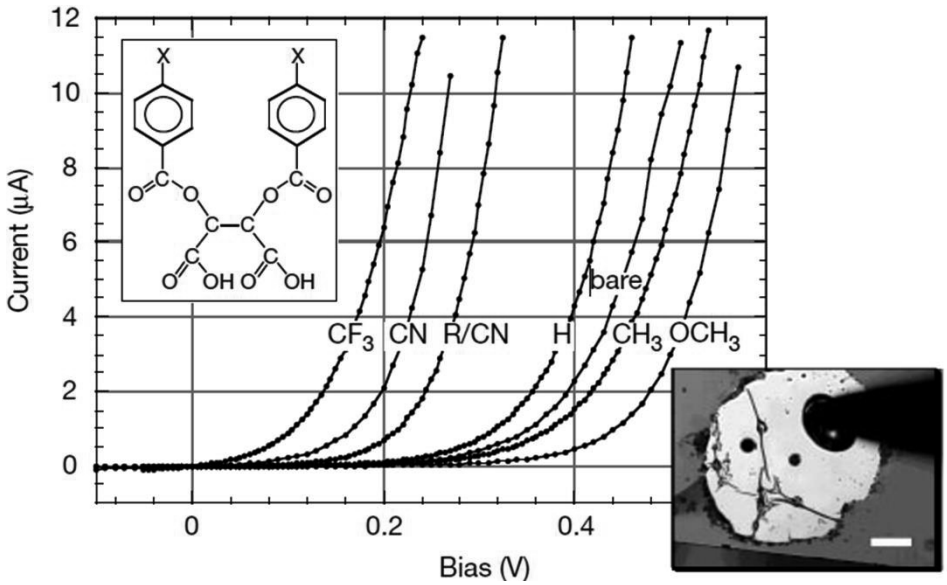

Figure 1.8 Electrical characteristics of LOFO junctions. Main figure is the different *I-V* curves refer to the junctions of different substituent on the benzene ring (shown next to each curve) of the dicarboxylic acid derivatives (see inset). Bottom right inset is optical micrograph (scale bar, 100 μm) of Au pad [31]

Figure 1.8) are deposited on GaAs substrate. Systematic modification of the molecular dipole is possible by the substituted benzene groups with various substituents in this work. Compared to the control junction (bare), molecularly modified GaAs / Au diodes show the change in *I-V* characteristics depending on the direction and magnitude of each molecular dipoles. It is shown that the effective barrier height in diode junction is modified by the dipole moment of the substituted benzene, which results in changes in *I-V* characteristics. These barrier heights is also related to the work function of the surface but only limited fraction in the changed of work function are expressed in the effective barrier heights in the junctions based on GaAs substrate because the Schottky-Mott rule that used to extract the barrier

height in this work is not suitable tool for the covalent semiconductor like GaAs with high density of surface states. Later study, in which GaAs is replaced by ZnO (ionic semiconductor), shows the effective modulation in barrier heights depending on the work function of the surfaces treated by different molecules. [43]

(d) Electrode-transfer based on the polymer film

Another way to build top electrode on the molecular layer is to transfer the metal film with assistance of thin polymer film. The differentiations of this method from the imprinting technique are as follows; (i) ultra-flat surface of top electrode originates from the dummy substrate, (ii) surface chemistry to release the metal film from the stamp is less important since the polymer film is washed out when the junction is complete.

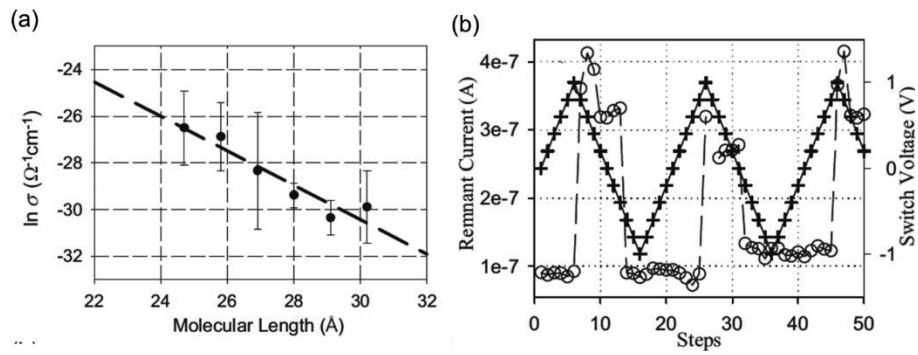

Figure 1.9 Electrical characteristics of PALO junctions. (a) Semi-log plot of the tunneling conductivity versus chain-length of fatty acid monolayers. The fit to a straight line gives a slope of β = 0.86 Å^{-1}. (b) Temporal plot of the remnant current (circles) as a function of applied bias (crosses), displaying switching behavior upon reaching a threshold voltage: 1 V for turning "on" and –0.6 V for turning "off". [32]

Figure 1.6(c) illustrates the fabrication procedure for one of these methods, termed as polymer-assisted lift-off (PALO). [32] Gold electrode is patterned on ultrasmooth, sacrificial substrate (Si or mica). Poly(methyl methacrylate) (PMMA) or poly(styrene) is then coated covering the whole surface. The electrodes with a PMMA film are detached from the dummy substrate by immersing the sample into the basic solution which weakens the adhesion between the polymer film and substrate. This film is then transferred onto the molecule-treated bottom electrode. After drying the common liquid (water), PMMA is removed by organic solvent. The wrinkle-free electrode is explained by the surface energies (γ) at each interface. Hydrophobicity of gold-PMMA film and molecular monolayer means the high surface energy (γ_{13} and γ_{23}) at the interface with water, which drives water out and

makes fine contact between top electrode and molecular layer. In this work, Fatty acids, $CH_3(CH_2)_{n-2}COOH$ with various molecular lengths are deposited on the bottom electrode by LB film method. The conductivity (σ) in the low bias regime can be expressed by a model for non-resonant tunneling, in which the conductivity is decayed exponentially as the width of tunneling barrier increases. This relationship can be approximately expressed by Simmons equations, where σ_0 is a constant that depends on the system and includes contact resistance, d (Å) is the width of the tunneling barrier, and β ($Å^{-1}$) is the decay coefficient.

$$\sigma = \sigma_0 e^{-\beta d} \qquad \text{Eq. 1.12}$$

Figure 1.9(a) is the semi-log plot of the conductivity versus the molecular lengths of fatty acids, which is consistent with the Simmons model. Molecular switching devices with a bistable [2]-rotaxane molecules is also demonstrated in the platform of PALO in which the conductivity is switched by the redox process inside the molecule. [44] Small bias is applied across the junctions to read 'remnant' current after write voltage pulse. Their switching property is shown in Figure 1.9(b), in which the current rapidly switches the states with the threshold voltages of 1 V for turning on and -0.6 V for turning off.

Figure 1.6(d) shows another example of polymer-assisted electrode transfer, termed as 'direct metal transfer (DMT)'[33]. This method is similar to PALO junction but the gold electrode transfer onto '*via*-hole' structure of which bottom gold electrode is exposed through the hole by etching the insulating layer. Alkanethiolates (denoted as C8, C12, and C16) are used in this work, and their electrical properties are investigated statistically (Figure 1.9(a) and (b)). The decay coefficient β (~ 1.07

$Å^{-1}$) and the current independent on the temperature (Figure 1.9(c) and (d)) imply that the dominant transport mechanism in these junctions is the non-resonant tunneling which follows the Simmons model. The inelastic electron tunneling spectroscopy (IETS) in DMT junction was also measured.[45] IETS is one of the powerful tools for the detection of unique vibration modes of molecules in a tunneling junction. This spectroscopy captures the specific vibration mode of the molecule when electrons tunnel inelastically by delivering an energy quantum into a localized vibrational mode of the molecule. At the specific voltage there appears IETS peak in the second derivative of current versus voltage (d^2I/dV^2-V) graph. Figure 1.10(e) shows the positions of vibration modes in several DMT junctions of C12 molecule, which are consistent with the other studies for IETS measurement of molecular junctions with alkanethiolates[10,11,46–48].

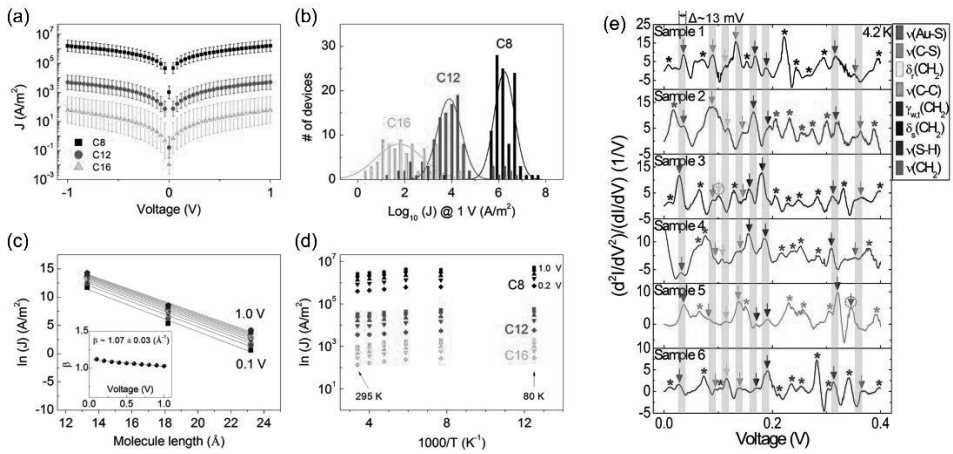

Figure 1.10 Electrical characteristics of DMT junctions. (a) Statistical *J–V* data for C8, C12, and C16 working devices. (b) Distribution of the logarithmic current densities at 1 V for all molecular junctions. (c) A semi-log plot of the current densities measured at different biases as a function of the molecular length. Solid lines represent the exponential fitting results, in which the slope is related to the decay coefficient β. The inset shows the values of β deduced from the plot versus the applied bias. (d) Arrhenius plot of the logarithmic current densities for C8, C12 and C16 molecular junctions at different biases from 0.2 V to 1.0 V in 0.2 V increments. The temperature was varied from 80 K to 295 K in 40 K increments [33]. (e) IETS data of six C12 molecular junctions measured at 4.2 K. Each arrow indicates the corresponding molecular vibration modes of the C12 molecule. Peaks that cannot be assigned to any possible vibrational modes of the molecule are marked with asterisks. In this plot, shaded squares are used to compare each characteristic peak from device to device[45].

1.3.4. Reliable Molecular Electronic Junctions with a Multilayer Graphene Electrode

(a) Overview

Graphene is an ultra-thin two-dimensional sheet of covalently bonded carbon atoms with outstanding electronic properties, chemical stability and mechanical material properties. It is considered to be a good electrode candidate for molecular junctions. Furthermore, large-area, conductive and flexible graphene films have been successfully synthesized by chemical vapor deposition (CVD) method, with the ability to patterning or creation of a desired size and shape of the film. As mentioned in the previous section, the limitations of the vertical type molecular junctions are their low device yield and hardness to define molecule-electrode interfaces' nature. The low yield of the molecular junction is attributed to metal penetration within top electrode deposition. As an alternative approach to prevent metal penetration, inserting graphene electrode as an interlayer top electrode as a protective layer before top metal evaporation. In particular, molecular electronic junctions using multilayer graphene (MLG) film as a transferred top electrode have demonstrated a reliable device yield and stability over time[34,35]. In this chapter, I summarize the approach for fabricating solid-state molecular monolayer junctions with MLG electrodes and its charge transport characteristics.

The fabrication process of MLG electrode molecular junctions is followed by the same process for other via-hole structure solid-state vertical junctions. Figure 1.11 shows the device fabrication procedure. Given bottom electrode patterns on a substrate, via-holes were created by optical lithography. The MLG film transferred

onto the hole where self-assembled monolayer (SAM) deposited on the bottom electrode. The MLG film can be obtained by using MLG grown on Ni or by repeated transfer of single layer graphene grown on Cu. Deposition of the top metal pad is followed. If single-layer graphenes were used as the interlayer instead of MLG, the evaporated metal atoms might penetrate in this step due to the cracks or pores generated in their growth and transfer processes, which results in the low yield of the molecular junctions.

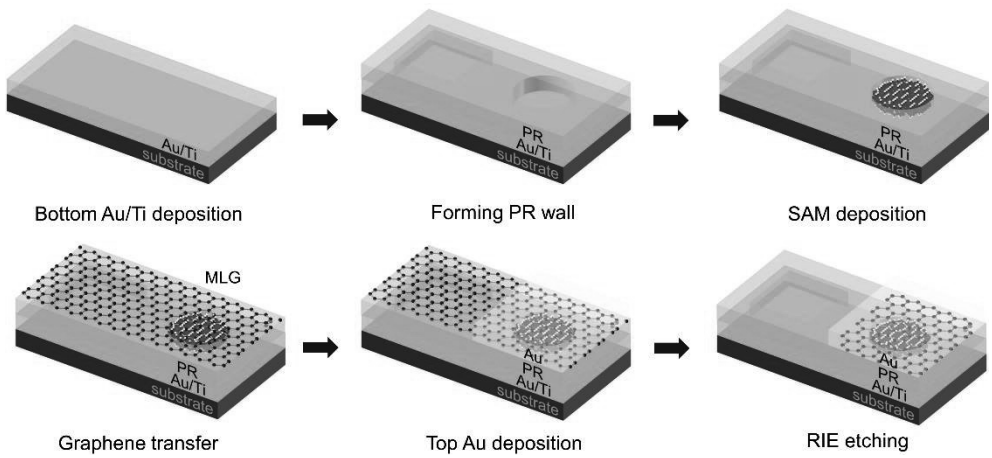

Figure 1.11 Schematic illustration of the device fabrication process for the graphene electrode molecular junctions [35].

(b) Electrical characterization

The typical way to verify that molecular junction with given structure is reliable is to statistically investigate electrical characteristics of device with test-bed molecules such as alkanethiolates or benzenethiolates. Figure 1.12(a) shows statistical current density-voltage (*J*-*V*) characteristics for the alkanemonothiol (C8,

C12, and C16) and alkanedithiol (DC8) molecular junctions and Figure 1.12(b) shows the same for benzenedithol (BDT, BPDT, TPDT) molecular junctions with MLG electrodes. Charge transport mechanism across SAMs of alkanethiolates or benzenethiolates follows the Simmons model mentioned above. As depicted in Figure 1.12(c), the decay coefficient β can be easily calculated in the log(J)-V curve, where its absolute value of slope is the same as β. The obtained β value for alkanethiols was about 0.85 $Å^{-1}$, while 0.33 $Å^{-1}$ for benzenedithiolates. These matches well with reference β values.[5,10,49–55] With temperature-varying current density-voltage (J-V-T) measurement, alkanethiolate and benzenethiolate molecular junctions exhibit temperature-independent J-V, which imply that the primary mechanism of charge transport is non-resonant tunneling.[10,35,55] The durability and operational stability of device are crucial for the practical application. Molecular junctions with graphene electrode show excellent reliability that have long device lifetime without deterioration (more than 40 day), retention characteristics (over 10^4 sec). [34] The reliability of the same molecular junctions fabricated on flexible substrate was also demonstrated, under various bending conditions (Figure 1.12(d)). [35]

In addition to fundamental current-voltage characterization and temperature-varying measurements, IETS for BDT molecular junctions with graphene electrode was also successfully observed as shown in Figure 1.12(e). The IETS peaks are observed at 21, 82, 136, and 209 mV, all of which match with the intrinsic vibration modes of BDT.[11,47,56–58]

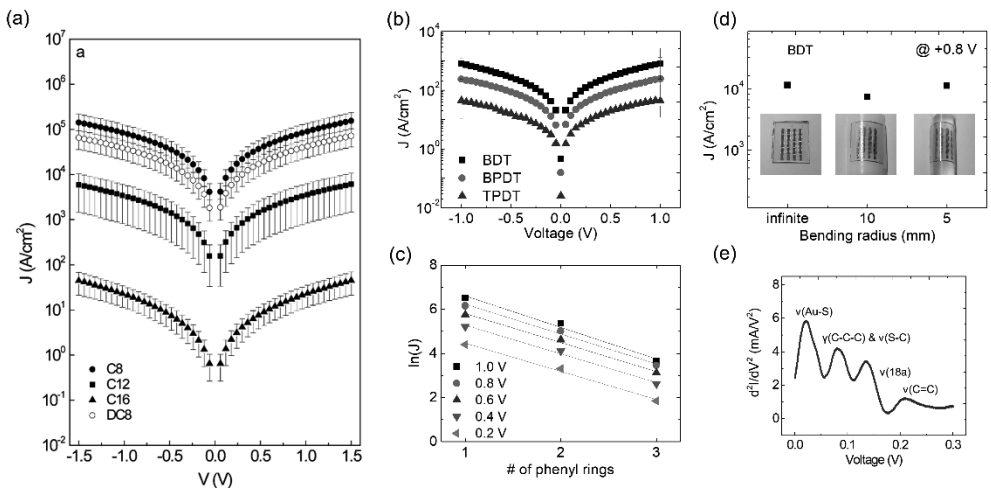

Figure 1.12 Statistical *J-V* data for all (a) C8, C12, C16 and DC8 molecular junctions [34], (b) BDT, BPDT, TPDT molecular junctions. (c) A semi-log plot of the *J* values at different biases versus the numbers of phenyl rings in the BDT, BPDT, and TPDT molecular junctions. (d) Current densities measured at 0.8 V in different bending configurations (bending radii of ∞, 10 mm, and 5 mm). (e) d^2I/dV^2 plot of a BDT molecular junction with a graphene electrode. In the d^2I/dV^2 plot, IETS peaks can be observed at 21, 82, 136, and 209 mV [35].

(c) Interface-Engineered Molecular Electronic Junctions with Chemically Doped Graphene Electrode

As mentioned above, it has been demonstrated that graphene is suitable electrode material for fabrication of reliable molecular junctions. Moreover, it is a promising candidate for interface engineering since its electronic structure can be easily modified by chemical treatment or other external stimuli. A representative

demonstration of interface engineering of graphene-electrode molecular junction was reported,[37] adopting chemical p-type doping method of a graphene film using trifluoromethanesulfonic acid (CF_3SO_3H, denoted as TFMS). It has been shown that solution-processed p-doping of graphene using TFMS provide high optical transmittance, low sheet resistance, high work function (0.83 eV increase), smooth surface, and air-stability.[59] Figure 1.13(a) shows the schematic illustration of TFMS-doped graphene.

The molecular junctions were fabricated with benzene-1,4-dithiol (BDT) self-assembled monolayers with pristine (work function of ~4.4 eV) and TFMS-treated p-doped (work function of ~5.23 eV) graphene. From statistical analysis, noticeably enhanced charge transport properties and lowered transport barriers for the TFMS-treated p-doped graphene-electrode BDT molecular junctions were observed. These phenomena originate from increased hole concentration and decreased hole injection barrier at the graphene-BDT interface because the main charge transport mechanism of the junction is highest occupied molecular orbital (HOMO)-mediated non-resonant tunneling. In that study, a sufficient number of molecular junctions were fabricated with pristine multilayer graphene/BDT/Au (denoted as graphene/BDT/Au) and TFMS-doped multilayer graphene/BDT/Au (denoted as TFMS-graphene/BDT/Au) structures. The molecular junctions consisting of the TFMS-doped graphene electrode have been successfully fabricated with a reliable yield (> 70%), Figure 1.13(b) and (c) show 2-dimensional current density-voltage (*J-V*) plots of all working molecular junctions for the graphene/BDT/Au junctions and TFMS-graphene/BDT/Au junctions. The average current density was increased about one

order of magnitude for the TFMS-doped graphene-electrode molecular junctions compared to that of the pristine graphene-electrode molecular junctions. Transition voltage spectroscopy (TVS) reveals the effective barrier (i.e., the offset between the Fermi energy of the electrode (E_F) and energy level of the HOMO (E_{HOMO})) for electron to tunnel the molecule-electrode interface. The threshold voltage V_T can be obtained from the inflection point of the Fowler-Nordheim plot, which equals the barrier height when applying the Simmons tunneling model.[60,61] As a result of TVS for the graphene/BDT/Au molecular junctions, the average value of V_T was found to be ~1.08 V and was symmetric for positive and negative voltage polarities. On the other hand, the averaged value of V_T for TFMS-graphene/BDT/Au junctions was found to be ~0.78 V for both voltage polarities, which was ~0.3 V lower than that of the graphene/BDT/Au junctions. These results imply that the work function increase of the p-doped graphene electrode lowered the charge injection barrier in the HOMO-dominating molecular tunnel junctions.

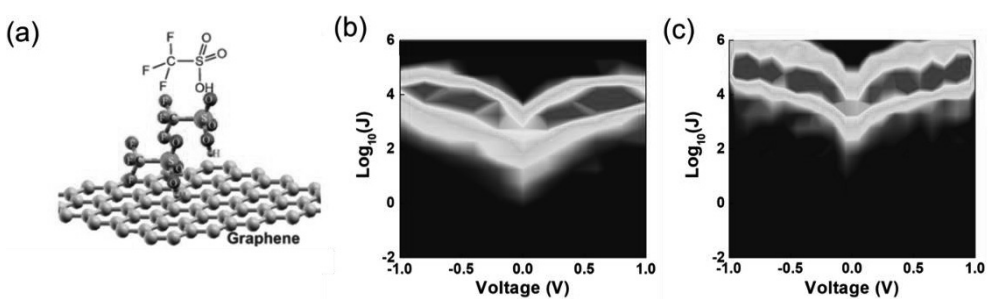

Figure 1.13 (a) Chemical structure of trifluoromethanesulfonic acid (TFMS) (top) and schematic illustration of TFMS-doped graphene (bottom) [59]. Two-dimensional *J-V* plots of the working molecular junctions for the (b) graphene/BDT/Au and (c) TFMS-graphene/BDT/Au junctions [37].

3.4 Photoswitching molecular junctions with graphene electrodes

To achieve the practical application of molecular electronic devices, a wide range of studies in functional molecular electronics has been carried out over the last decades. One of the most important developments for utilization of functional molecules is photoswitching molecular junctions. Light is useful source for switching devices because of its addressability and compatibility with solid-state device structures. Therefore, the design of photochromic molecules is important for molecular switching devices. In particular, diarylethene (DAE) has been utilized in various ways with the aim to demonstrate bidirectional switching in molecular junctions. DAEs form a class of photochromes with two different conductance states, i.e., a high conductance (closed; ON) and a low conductance (open; OFF) state. In solution, DAEs can be converted between these two states by illumination with UV or visible light, respectively. This property makes them good candidates for photoswitching molecular junctions due to a large conductance difference between the two states and their response to light.[22,36,62–66] However, the switching behavior of DAE molecular junctions bridged by metal electrodes has been elusive. For example, an Au-DAE-Au junction was only exhibited a unidirectional switching from the closed to the open state.[64] This result is attributed to the quenching of the excited state of the DAE due to strong electronic coupling between the Au metal and the sulfur-based end group, thereby hindering the molecule to adopt its high conductance state. [65] On the other hand, unidirectional switching from the low- to the high-conductance state in Au-DAE-Au single-molecule junctions was obtained by modifying the side-arms and end-groups such that they form rigid conjugated

molecular wires.[67] These molecules feature a very high quantum yield for the ON switching reaction, but a relatively low one for the OFF switching, explaining the inversed unidirectional switching. In addition, a similar single DAE molecule, bridged between carbon nanotubes[63] or graphene sheets[68] showed a unidirectional switching from the open to the closed state, because strong molecule-electrode couplings between closed state DAE and graphene electrodes enabled the energy transfer from the photoexcited molecule to the extended π-electron system in the electrodes.[69,70]

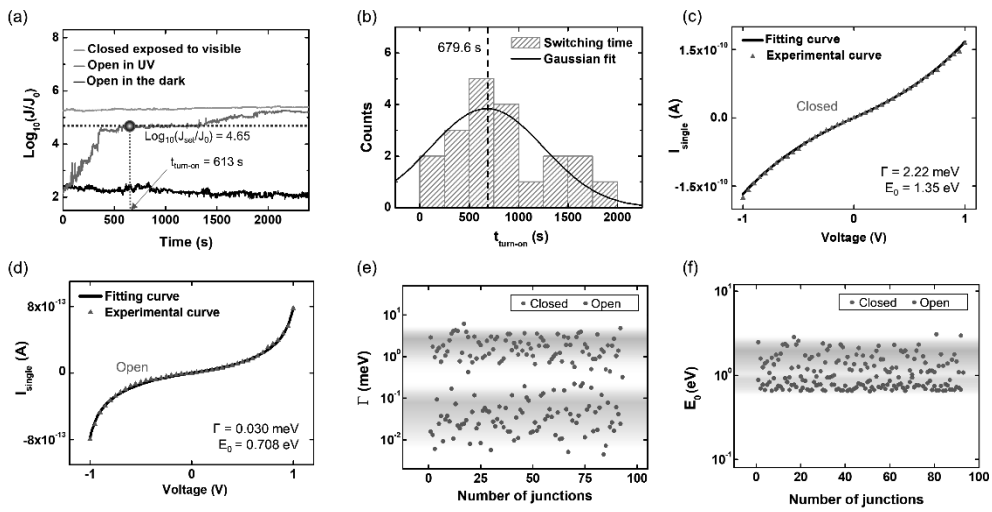

Figure 1.14 (a) Real-time measurement of the current density for each state with or without exposure to light at an applied bias voltage of 1 V. The switching time (turn-on) is indicted by an arrow. (b) Histogram for the measured switching time required to transition from the open to the closed state. A representative single *I-V* curve measured for the (c) closed and (d) open state, with the fitting curve (shown as a solid line) calculated based on the Landauer formula. Scatter point plots for (e) Γ and (f) E_0 values for intact molecular junctions in the closed and open state [36].

In recent study, charge transport characteristics of DAE photoswitching molecular junction with MLG electrode were reported. [36] The authors have found that the device can only be switched from the OFF to the ON state, i.e., from the open to the closed state of the employed 1,2-bis(2-methyl-5-(4-mercaptophenylethynyl)furan-3-yl)perfluorcyclopent-1-ene (DAE). Figure 1.14(a) shows the phototransition properties of the DAE molecular junctions with MLG electrode by real-time current density (*J-t*) measurements. Each data means the open state in the dark (black line), open state exposed to 15 mW UV light (purple line), and closed state exposed to visible light (green line) with the same intensity as the UV light. The current level of the junction in the open state in the dark showed no changes, which suggests that the bias voltage applied to the molecular junction cannot induce the switching. In addition, for the case of the molecular junction prepared in the closed state, the switching behavior could not be observed when exposed to visible light. The only switching behavior that could observe was unidirectional switching from open to closed state. The average switching time was around 680 s, as shown in Figure 1.14(b). Note that switching behavior of the DAE molecule is not precisely defined but stochastic and its shape is quite variate among samples.

Figure 1.14(c) and (d) show the fitting curve of experimental I_{exp}-V data with Landauer formalism. The approximate current I_{single} through an equivalent single-molecule junction could be given as

$$I_{\text{single}} = \frac{c}{NA} I_{\text{exp}} = \frac{2e}{h} \int_{-\infty}^{\infty} dE\, T(E)\, [f_L(E) - f_R(E)] \qquad \text{Eq. 1.13}$$

Here, $f_X(E)$ is the Fermi-Dirac distribution function, where μ_X is the chemical

potential of the electrode *X* = top or bottom. Another factors, *N* is molecular coverage, *c* is phenomenological factor that offsets discrepancy between single molecular junction and SAM junction. The *T(E)* is a transmission function that was given by single-level symmetric Lorentzian function as below.

$$T(E) = \frac{\Gamma^2}{(E - E_0)^2 + \Gamma^2} \qquad \text{Eq. 1.14}$$

The E_0 is the difference between the eigen energy of frontier orbital and the Fermi energy of electrode. And Γ indicates the electronic coupling strength of the molecular orbital to the respective electrode. By performing numerical curve fitting, one can calculate the factor E_0 and Γ from each *I-V* curve. Figure 1.14(c) shows curve fitting result of closed state molecular junction, whereas Figure 1.14(d) shows result for open state molecular junction. For all working junctions, the distribution of Γ and E_0 values are presented in the scatter plot in Figure 1.14(e) and (f). By averaging these distributions, the effective coupling strength Γ for closed and open states was determined to be 1.93 meV and 0.0572 meV, respectively, and the corresponding charge injection barrier E_0 for closed and open states was extracted to be 1.560 meV and 0.756 meV, respectively. In particular, it is notable that the effective value of Γ in the closed state is more than 30 times larger than that of the open state. The relatively strong coupling between DAE and MLG electrodes in the closed state may also cause the unidirectional switching. It is possible that the strong interaction between the closed state of the DAE molecules and the electrode can quench the photo-excited closed state, effectively disturbing the switching process and eventually preventing the transition to the open state.[36,64,71,72]

References

[1] A. Aviram, M. A. Ratner, *Chem Phys Lett* **1974**, *29*, 277.

[2] R. Landauer, *Ibm J Res Dev* **1957**, *1*, 223.

[3] J. Cuevas, E. Scheer, *Eur Mat Res* **2010**, 623.

[4] J. Simmons, *J Appl Phys* **1963**, *34*, 1793.

[5] S. H. Choi, B. Kim, C. D. Frisbie, *Science* **2008**, *320*, 1482.

[6] C. Vericat, M. Vela, G. Benitez, P. Carro, R. Salvarezza, *Chem Soc Rev* **2010**, *39*, 1805.

[7] B. Xu, X. Xiao, N. J. Tao, *J Am Chem Soc* **2003**, *125*, 16164.

[8] F. Chen, J. Hihath, Z. Huang, X. Li, N. J. Tao, *Annu Rev Phys Chem* **2007**, *58*, 535.

[9] D. Wold, C. Frisbie, *J Am Chem Soc* **2001**, *123*, 5549.

[10] H. Song, Y. Kim, H. Jeong, M. A. Reed, T. Lee, *J Appl Phys* **2011**, *109*, 102419.

[11] H. Song, Y. Kim, Y. H. Jang, H. Jeong, M. A. Reed, T. Lee, *Nature* **2009**, *462*, 1039.

[12] J. Park, A. N. Pasupathy, J. I. Goldsmith, C. Chang, Y. Yaish, J. R. Petta, M. Rinkoski, J. P. Sethna, H. D. Abruña, P. L. McEuen, D. C. Ralph, *Nature* **2002**, *417*, 722.

[13] M. A. Reed, C. Zhou, C. J. Muller, T. P. Burgin, J. M. Tour, *Science* **1997**, *278*, 252.

[14] D. Xiang, H. Jeong, D. Kim, T. Lee, Y. Cheng, Q. Wang, D. Mayer, *Nano*

Lett **2013**, *13*, 2809.

[15] L. Venkataraman, J. Klare, C. Nuckolls, M. Hybertsen, M. Steigerwald, *Nature* **2006**, *442*, 904.

[16] J. Love, L. Estroff, J. Kriebel, R. Nuzzo, G. Whitesides, *Chem Rev* **2005**, *105*, 1103.

[17] B. Mann, H. Kuhn, *J Appl Phys* **1971**, *42*, 4398.

[18] E. E. Polymeropoulos, J. Sagiv, *J Chem Phys* **1978**, *69*, 1836.

[19] A. V. Walker, T. B. Tighe, O. M. Cabarcos, M. D. Reinard, B. C. Haynie, S. Uppili, N. Winograd, D. L. Allara, *J Am Chem Soc* **2004**, *126*, 3954.

[20] Z. Zhu, D. Allara, N. Winograd, *Appl Surf Sci* **2006**, *252*, 6686.

[21] H. B. Akkerman, P. W. M. Blom, D. M. de Leeuw, B. de Boer, *Nature* **2006**, *441*, 69.

[22] D. Kim, H. Jeong, H. Lee, W. Hwang, J. Wolf, E. Scheer, T. Huhn, H. Jeong, T. Lee, *Adv Mater* **2014**, *26*, 3968.

[23] H. Jeong, D. Kim, G. Wang, S. Park, H. Lee, K. Cho, W. Hwang, M. Yoon, Y. H. Jang, H. Song, D. Xiang, T. Lee, *Adv Funct Mater* **2014**, *24*, 2472.

[24] C. A. Nijhuis, W. F. Reus, J. R. Barber, M. D. Dickey, G. M. Whitesides, *Nano Lett* **2010**, *10*, 3611.

[25] L. Yuan, L. Jiang, D. Thompson, C. Nijhuis, *J Am Chem Soc* **2014**, *136*, 6554.

[26] L. Jiang, C. S. S. Sangeeth, A. Wan, A. Vilan, C. A. Nijhuis, *J Phys Chem C* **2014**, *119*, 960.

[27] W. Wang, T. Lee, M. A. Reed, *Phys Rev B* **2002**, *68*, 035416.

[28] T. Kim, G. Wang, T. Lee, *Ieee T Nanotechnol* **2008**, *7*, 140.

[29] C. Nijhuis, W. Reus, G. Whitesides, *J Am Chem Soc* **2009**, *131*, 17814.

[30] Y.-L. Loo, D. V. Lang, J. A. Rogers, J. W. P. Hsu, *Nano Lett* **2003**, *3*, 913 917.

[31] A. Vilan, A. Shanzer, D. Cahen, *Nature* **2000**, *404*, 166.

[32] K. T. Shimizu, J. D. Fabbri, J. J. Jelincic, N. A. Melosh, *Adv Mater* **2006**, *18*, 1499 1504.

[33] H. Jeong, D. Kim, P. Kim, M. R. Cho, W.-T. Hwang, Y. Jang, K. Cho, M. Min, D. Xiang, Y. D. Park, H. Jeong, T. Lee, *Nanotechnology* **2015**, *26*, 025601.

[34] G. Wang, Y. Kim, M. Choe, T. Kim, T. Lee, *Adv Mater* **2011**, *23*, 755.

[35] Y. Jang, H. Jeong, D. Kim, W.-T. Hwang, J.-W. Kim, I. Jeong, H. Song, J. Yoon, G.-C. Yi, H. Jeong, T. Lee, *Nanotechnology* **2016**, *27*, 145301.

[36] J. Koo, Y. Jang, L. Martin, D. Kim, H. Jeong, K. Kang, W. Lee, J. Kim, W.-T. Hwang, D. Xiang, E. Scheer, M. Kabdulov, T. Huhn, F. Pauly, T. Lee, *Acs Appl Mater Inter* **2019**, *11*, 11645.

[37] Y. Jang, S.-J. Kwon, J. Shin, H. Jeong, W.-T. Hwang, J. Kim, J. Koo, T. Y. Ko, S. Ryu, G. Wang, T.-W. Lee, T. Lee, *Acs Appl Mater Inter* **2017**, *9*, 42043.

[38] C. Zhou, M. R. Deshpande, M. A. Reed, L. Jones, J. M. Tour, *Appl Phys Lett* **1997**, *71*, 611.

[39] J. Chen, M. A. Reed, A. M. Rawlett, J. M. Tour, *Science* **1999**, *286*, 1550.

[40] H. Haick, D. Cahen, *Accounts Chem Res* **2008**, *41*, 359.

[41] A. Vilan, D. Cahen, *Adv Funct Mater* **2002**, *12*, 795 807.

[42] Y. Selzer, D. Cahen, *Adv Mater* **2001**, *13*, 508.

[43] A. Salomon, D. Berkovich, D. Cahen, *Appl Phys Lett* **2003**, *82*, 1051.

[44] C. P. Collier, J. O. Jeppesen, Y. Luo, J. Perkins, E. W. Wong, J. R. Heath, J. F. Stoddart, *J Am Chem Soc* **2001**, *123*, 12632.

[45] H. Jeong, W.-T. Hwang, P. Kim, D. Kim, Y. Jang, M. Min, D. Xiang, H. Song, Y. D. Park, H. Jeong, T. Lee, *Appl Phys Lett* **2015**, *106*, 063110.

[46] N. Okabayashi, Y. Konda, T. Komeda, *Phys Rev Lett* **2008**, *100*, 217801.

[47] W. Wang, T. Lee, I. Kretzschmar, M. A. Reed, *Nano Lett* **2004**, *4*, 643.

[48] Y. Kim, T. Pietsch, A. Erbe, W. Belzig, E. Scheer, *Nano Lett* **2011**, *11*, 3734.

[49] B. Xu, N. J. Tao, *Science* **2003**, *301*, 1221.

[50] T.-W. Kim, G. Wang, H. Lee, T. Lee, *Nanotechnology* **2007**, *18*, 315204.

[51] N. Tao, *Nat Nanotechnol* **2006**, *1*, 173.

[52] H. B. Akkerman, B. de Boer, *J Phys Condens Matter* **2008**, *20*, 013001.

[53] V. Engelkes, J. Beebe, C. Frisbie, *J Am Chem Soc* **2004**, *126*, 14287.

[54] F. Chen, X. Li, J. Hihath, Z. Huang, N. Tao, *J Am Chem Soc* **2006**, *128*, 15874.

[55] D. Wold, R. Haag, M. Rampi, C. Frisbie, *J Phys Chem B* **2002**, *106*, 2813.

[56] P. Hansma, *Phys Reports* **1977**, *30*, 145.

[57] C. J. Adkins, W. A. Phillips, *J Phys C Solid State Phys* **2000**, *18*, 1313.

[58] L.-L. Lin, C.-K. Wang, Y. Luo, *Acs Nano* **2011**, *5*, 2257.

[59] T. Han, S. Kwon, N. Li, H. Seo, W. Xu, K. S. Kim, T. Lee, *Angewandte Chemie Int Ed* **2016**, *55*, 6197.

[60] J. M. Beebe, B. Kim, C. D. Frisbie, J. G. Kushmerick, *Acs Nano* **2008**, *2*, 827.

[61] J. M. Beebe, B. Kim, J. W. Gadzuk, C. D. Frisbie, J. G. Kushmerick, *Phys Rev Lett* **2006**, *97*, 026801.

[62] M. Irie, S. Kobatake, M. Horichi, *Science* **2001**, *291*, 1769.

[63] A. C. Whalley, M. L. Steigerwald, X. Guo, C. Nuckolls, *J Am Chem Soc* **2007**, *129*, 12590.

[64] D. Dulić, S. J. van der Molen, T. Kudernac, H. T. Jonkman, J. J. D. de Jong, T. N. Bowden, J. van Esch, B. L. Feringa, B. J. van Wees, *Phys Rev Lett* **2003**, *91*, 207402.

[65] M. Zhuang, M. Ernzerhof, *J Chem Phys* **2009**, *130*, 114704.

[66] A. J. Kronemeijer, H. B. Akkerman, T. Kudernac, B. J. van Wees, B. L. Feringa, P. W. M. Blom, B. de Boer, *Adv Mater* **2008**, *20*, 1467.

[67] T. Sendler, K. Luka-Guth, M. Wieser, Lokamani, J. Wolf, M. Helm, S. Gemming, J. Kerbusch, E. Scheer, T. Huhn, A. Erbe, *Adv Sci* **2015**, *2*, 1500017.

[68] S. J. van der Molen, J. Liao, T. Kudernac, J. S. Agustsson, L. Bernard, M. Calame, B. J. van Wees, B. L. Feringa, C. Schönenberger, *Nano Lett* **2009**, *9*, 76.

[69] C. Jia, A. Migliore, N. Xin, S. Huang, J. Wang, Q. Yang, S. Wang, H. Chen, D. Wang, B. Feng, Z. Liu, G. Zhang, D.-H. Qu, H. Tian, M. A.

Ratner, H. Q. Xu, A. Nitzan, X. Guo, *Science* **2016**, *352*, 1443.

[70] C. Jia, J. Wang, C. Yao, Y. Cao, Y. Zhong, Z. Liu, Z. Liu, X. Guo, *Angewandte Chemie Int Ed* **2013**, *52*, 8666 8670.

[71] M. J. Comstock, N. Levy, A. Kirakosian, J. Cho, F. Lauterwasser, J. H. Harvey, D. A. Strubbe, J. M. J. Fréchet, D. Trauner, S. G. Louie, M. F. Crommie, *Phys Rev Lett* **2006**, *99*, 038301.

[72] C. Gahl, R. Schmidt, D. Brete, E. R. McNellis, W. Freyer, R. Carley, K. Reuter, M. Weinelt, *J Am Chem Soc* **2010**, *132*, 1831.

Chapter 2. Gate-Dependent Asymmetric Characteristics in Pentacene Barristor

2.1. Introduction

Since its discovery, graphene has attracted considerable attention due to its advantageous properties, such as high carrier mobility, good mechanical properties, and chemical stability[1–6]. However, graphene has a fundamental limitation for use as an active channel in semiconductor devices such as field effect transistors (FETs) because of its zero-band gap feature. However, graphene's outstanding features of high conductivity, good flexibility, and transparency have led to it being explored for use as an electrode in various electrical and optical devices, including FETs[7–9], light-emitting diodes (LEDs) [10,11], and photovoltaic devices [12,13]. For example, Han et al. demonstrated flexible organic light-emitting diodes with extremely high luminous efficiency by introducing graphene sheets with a high work function in place of the conventional indium tin oxide (ITO) electrodes[11]. We also previously demonstrated that pentacene organic thin film transistors (OTFTs) with graphene electrodes exhibited an enhanced charge injection property with a reduced contact resistance compared to devices with typical Au electrodes[8].

In most cases, OTFTs are fabricated in the form of a horizontal FET device structure, in which two side regions across the organic channel layer are contacted by the source and drain electrodes from the bottom or from the top (called bottom-contact or top-contact OFETs, respectively). In contrast, alternative vertical

structures of FET devices with graphene electrodes have been demonstrated. The vertically stacked FET structure consists of gate / oxide / graphene / semiconductor / metal, and it is called a vertical FET (VFET) or barristor, in which a graphene film and metal (or another graphene film) are used as the bottom and top electrodes, respectively[14–17]. The charge injection barrier built within the graphene/channel interface can be effectively modulated by the electric field induced by the gate bias because the Fermi level of the semiconductor layer is not pinned to the Fermi level of graphene. Various semiconducting materials, such as silicon, molybdenum disulfide (MoS2), tungsten disulfide (WS2), and amorphous indium gallium zinc oxide (\alpha-IGZO), have been utilized in the VFET structure and exhibited a decent current modulation by the gate bias. For example, MoS2 VFETs with graphene electrodes showed transistor action with an on-off current ratio of 101–103 depending on the channel thickness at room temperature[16]. Organic films have also been applied as the channel in graphene-electrode VFET devices[18]. Ojeda-Aristizabal et al. demonstrated gate tunability in pentacene 'barristor' with graphene electrodes[18]. These authors demonstrated a gate-induced current modulation with a factor of 4 in response to changes in the gate bias from −50 to 50 V. Although a preliminary study of the electrical characteristics of graphene-electrode pentacene barristor has been performed, a more thorough analysis and understanding are desired, particularly in terms of the effect of asymmetric barrier contacts in the graphene/pentacene/Au barristor structure.

Herein, I independently investigated pentacene barristors with graphene and Au electrodes. I measured and analyzed the electrical transport characteristics of the

barristors by focusing on the properties originating from the asymmetric electrical contacts in the graphene/pentacene/Au structure. I also investigated the conduction mechanisms by considering the contribution of the bias voltage applied between graphene and Au and gate bias to the activation energies of interfacial trap sites.

2.2. Experiments

2.2.1. Device fabrication process

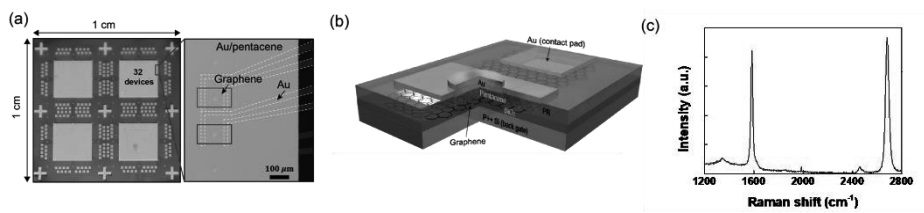

Figure 2.1 (a) The optical microscopy image (left) and scanning electron microscopy image (right) of the pentacene barristors. (b) The schematic image of the pentacene barristor. The bias voltage is applied to the graphene electrode, and p^{++} Si serves as the gate electrode. (c) Raman spectrum of the graphene film used as an electrode of the device.

Figure 2.1(a) presents optical microscopy and scanning electron microscopy images of the pentacene barristors, and Figure 2.1(b) presents a schematic image of the device structure. These devices consist of vertical heterojunction of graphene/pentacene/Au on Si/SiO_2 substrate. I fabricated this pentacene barristors by following procedures. First, I prepared a silicon substrate (1.5 cm × 1.5 cm) of a 270-nm-thick SiO_2 layer on a heavily doped p^{++} Si wafer (resistivity ~5×10^{-3} Ω cm) that can be used as a back gate. Au (30 nm thick)/Ti (5 nm thick) metal layers were

deposited and patterned on the substrate using an e-beam evaporator and a conventional photo-lithography technique, which will be used as a probing pad for the graphene electrode film. For the graphene electrode film, a single-layer graphene sheet was grown on a Cu foil (~10 cm × 10 cm) using the chemical vapor deposition (CVD) method. The grown graphene sheet was detached from the Cu foil using a wet transfer process and transferred to the substrate that contained pre-patterned Au contact pads. I patterned the transferred graphene sheet into small rectangular-shaped patches (200 μm × 100 μm, black line in Figure 2.1(a), right) using photolithography and oxygen plasma etching processes to create the desired contacts with the Au contact pads. Figure 2.1(c) shows the Raman spectrum of a graphene film that was transferred onto a Si/SiO_2 substrate. The Raman data suggest that the synthesized graphene film is a monolayer graphene film. Defect generated in synthesis or transferring process may be responsible for the rather high G peak compared to the 2D peak. Note that water or oxygen attached on graphene could work as defects so the graphene layer slightly exhibited *p*-type behaviors. Next, the isolation wall was created with a photoresist layer (AZ5214) by photolithography. This photoresist (PR) wall was created for preventing a direct charge pathway between bottom and top electrodes. I created vertical holes with a radius of 10 μm such that the graphene was revealed. Following this process, Pentacene (500 nm thick) was deposited on the substrate using a thermal evaporator at a rate of ~0.5 Å/s. Finally, the top Au (50 nm thick) electrode was formed on the pentacene layer using an e-beam evaporator and shadow masks. Figure 2.2 illustrates the procedures of the device fabrication.

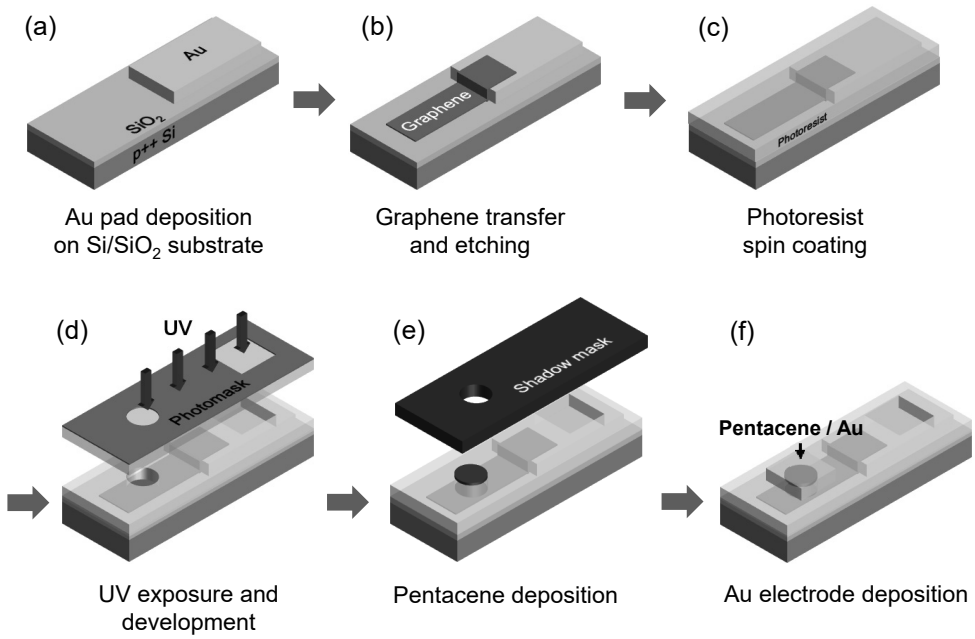

Figure 2.2 Fabrication processes of the pentacene barristor with graphene electrodes.

The Figure 2.3 illustrates the energy level information of the device. The work function of each electrode and the molecular orbital levels of pentacene. Note that the Fermi level of graphene can be modulated by gate bias up to 300 meV.

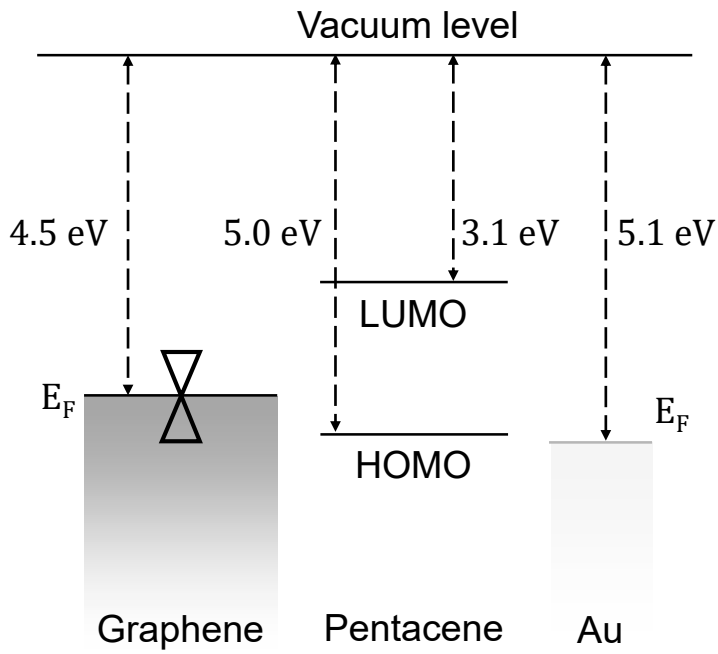

Figure 2.3 The energy level information for the device. The energy level alignment by the interfacial dipole layer discussed in main text is not featured in this figure.

2.2.2. Device characterization

I measured all the electrical characteristics of the pentacene barristors with the temperature-variable probe station (JANIS, ST-500) and the semiconductor parameter analyzer (Keithley, 4200-SCS) under vacuum condition (~ 1 mTorr). The temperature cooled down by supplying the liquid nitrogen. The Au top electrode was connected to ground and the bias voltage (V_b) was applied between the top and bottom electrodes. The current measured at the graphene bottom electrode (I_b).

2.3. Results and Discussions

2.3.1. Asymmetric charge transport properties

Figure 2.4(a) and (b) show the representative current-voltage characteristics of a graphene-electrode pentacene barristor at room temperature. Figure 2.4(a) shows the output characteristics (the current versus the bias voltage; I_b–V_b) at various gate bias voltage (V_g) ranging from –80 V to 80 V with an interval of 20 V. In this plot, diode-like electrical characteristics were observed, that is, there was a larger current flow under positive V_b compared to that under negative V_b at zero gate bias. In addition, significant current modulation by gate bias was observed only in positive V_b. Figure 2.4(b) presents the transfer curves (the current versus gate bias; I_b–V_g) at two fixed V_b values of ±9 V. The current at the V_b of +9 V (red line) decreased when the gate bias increased. It should be noted that current modulation was dominantly attributed to the change of the Schottky barrier height by gate bias. In contrast, the current at the V_b of –9 V (black line) did not significantly change. This voltage-dependent asymmetric property originates from the vertical heterostructure of the graphene/pentacene/Au stack, in which the charge transport is affected by the energy barrier at the top contact (with Au) and bottom contact (with graphene) of pentacene. In particular, current modulation was observed at specific bias voltage range ($V_b > 0$ V) because only the barrier height at the graphene/pentacene interface was effectively varied by the gate field due to the low density of states of graphene near the Dirac point in contrast to the barrier at the interface adjacent to Au, which has numerous densities of states.

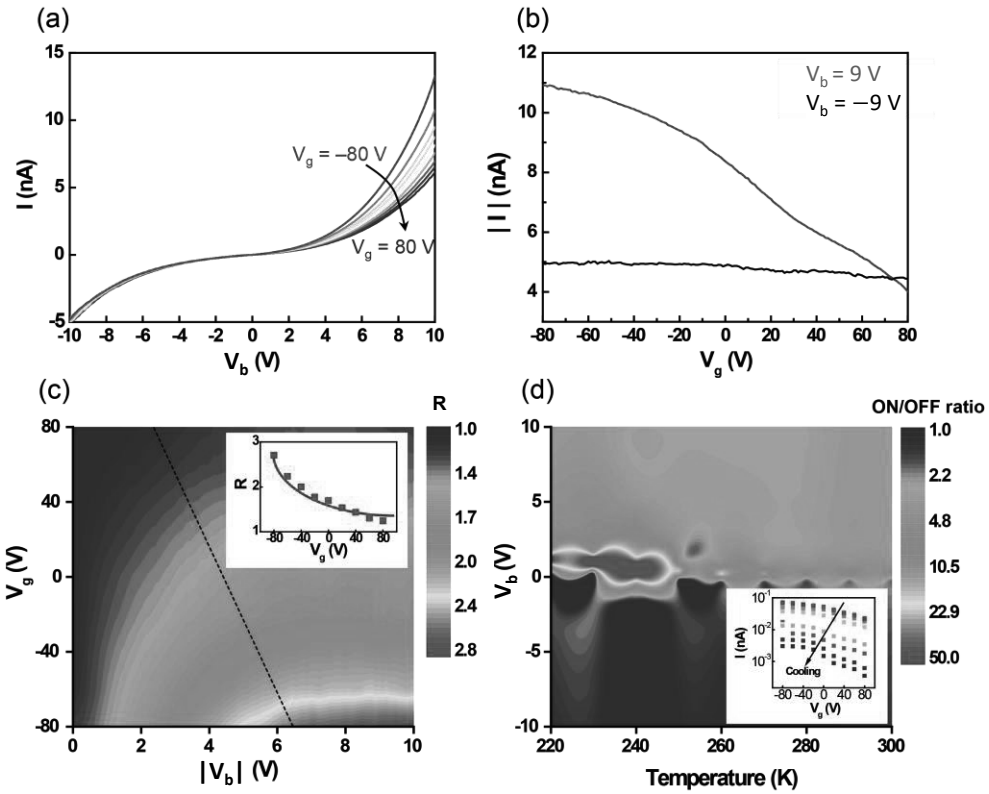

Figure 2.4 (a) The output characteristics (I_b-V_b) with V_b ranging from -10 V to 10 V at various V_g. (b) The transfer curves (I_b-V_g) of pentacene barristor at $V_b = \pm 9$ V. Both characteristics were measured as V_g increased from -80 V to 80 V. (c) Contour plot of the rectification ratio R = I_b ($V_b > 0$) / I_b ($V_b < 0$) within given V_b and V_g. The inset shows R versus V_g at V_b = 8 V. At fixed V_g, R was saturated in V_b higher than the values that are presented with a black dashed line. (d) Contour plot of ON/OFF ratio obtained from the *I-V-T* measurement. The inset shows transfer curves at various temperature conditions.

To investigate the rectifying property, I defined the rectification ratio (R) as the ratio between I_b (at positive V_b) and I_b (at negative V_b) and analyzed it within various

V_g and V_b at room temperature. This result is shown in Figure 2.4(c). The current rectification ratio increased up to 2.8 as $|V_b|$ increased and V_g decreased. The graphene electrode has remarkable advantages in aspect of the formation of distinct dipole layers compared to the use of the Au electrode built on each interface[8]. Pentacene, a *p*-type organic semiconductor, has its highest occupied molecular orbital (HOMO) located near the Fermi level of each electrode material, and thus, hole transport determines the current flow of this device. The pentacene layer deposited on graphene is stacked in a planar orientation through π-π interactions with graphene[22]. In this case, the interfacial dipole is formed at the graphene/pentacene junction interface such that it elevates the vacuum level of pentacene, resulting in lowering of the hole injection barrier[23,24]. In contrast, the dipole layer formed at the pentacene/Au junction interface raises the hole injection barrier[25,26]. The holes transport from the graphene to pentacene in the positive V_b range; thus, relatively large current flows due to the lowered hole injection barrier. Similarly, in the negative V_b range, smaller current flows because of the increased hole injection barrier from Au to pentacene. The exact energy barrier height can be estimated from variable-temperature electrical measurement, which will be discussed in a later section. This rectification ratio is also modulated as V_g varied because the current modulation occurs only in the positive V_b range (see Figure 2.4(b)). This gate-dependent rectification can be clearly observed in the inset of Figure 2.4(c), in which the rectification ratio was calculated as a function of V_g at a fixed $|V_b|$ = 8 V. Note that the rectification ratio linearly increased with $|V_b|$ but saturated above a certain bias voltage, as indicated by the green dashed line in Figure 2.4(c).

2.3.2. Barrier height modulation by the gate field

To further investigate the phenomena for the asymmetric properties in the current-voltage and current modulation characteristics, I conducted variable-temperature current-voltage (*I-V-T*) measurements while the temperature was changed from 220 to 280 K in increments of 10 K. The current modulation under various V_b and temperature conditions are presented in Figure 2.4(d), in which the ON/OFF ratio was defined as the ratio of I_b (V_g = –80 V) / I_b (V_g = 80 V). The ON/OFF ratio in the negative V_b range remained invariant due to little current modulation. However, for the positive V_b range, this ratio increased up to ~50 in the low temperature and low bias voltage region. The graphene/pentacene/Au stack can be considered to be two Schottky diodes reversely connected to each other. If the pentacene layer is fully depleted, then the Schottky barrier over which charge carriers inject from the electrode to pentacene determines the electrical characteristics of the entire junction[16,27,28]. Figure 2.5(a) and (b) show Arrhenius plots ($\ln(I_b/T^2)$ versus q/k_BT) for various gate biases from −80 to 80 V at a fixed V_b of ±2 V. A linear dependency was observed in these plots, which implies that the device obeys the thermionic emission as

$$I_b = AA^*T^2 \exp\left(-\frac{\phi_S - eV_b}{kT}\right) \qquad \text{Eq. 2.1}$$

where A is the junction area, A^* is the effective Richardson constant, and ϕ_S is the Schottky barrier height (i.e., the difference between the Fermi level of the electrode and the HOMO level of pentacene) that the holes cross over from the

electrode to pentacene.

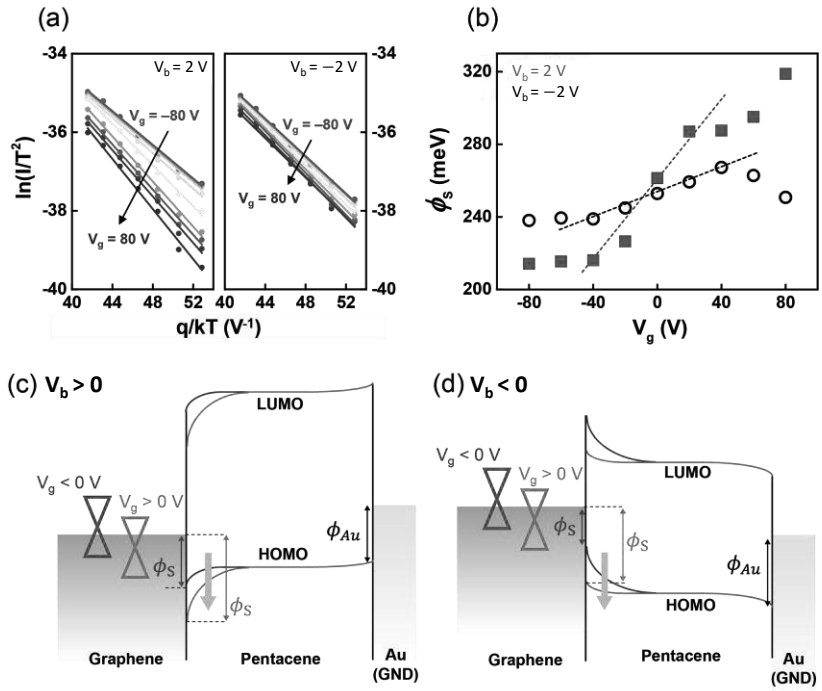

Figure 2.5 (a) Arrhenius plots at V_b = 2 V (left) and at V_b = –2 V (right), in which the slopes of each line correspond to the Schottky barrier height (ϕ_S). (b) Schottky barrier modulation by gate bias voltage at V_b = 2 V (red squares) and at V_b = –2 V (black circles). The dashed lines are the gradient of ϕ_S near V_g = 0 V. (c,d) The schematic band diagrams in the range of (c) $V_b > 0$ and (d) $V_b < 0$. The energy bands are expressed as red lines for $V_g < 0$ and blue lines for $V_g > 0$.

Therefore, the slopes of the fitting lines in right and left part of Figure 2.5(a) are related to the Schottky barrier at the graphene/pentacene and pentacene/Au interfaces, respectively. From these figures, one can observe that the slope, that is, the energy barrier, changed more by the gate bias at positive V_b (here, 2 V), whereas

the slopes of the Arrhenius plots did not change noticeably by the gate bias at negative V_b (here, –2 V). Although the bias voltage applied to the graphene bottom electrode affects the strength of electric field from the gate contact (i.e., by screening the gate electric field), this screening effect by the graphene electrode can be negligible because of the relatively small V_b compared to the large gate bias (up to 80 V). Figure 2.5(b) summarizes the energy barrier (ϕ_S) modulation induced by the gate bias, extracted from the slopes of the fitting lines in Figure 2.5(a). As shown in this plot, the barrier height changed from 220 to 320 meV at positive V_b, whereas only a negligible change was found for negative V_b. In the $V_b > 0$ range, in which the holes are injected into pentacene from the graphene electrode, the charge injection barrier that the holes have to pass through was tuned by the gate field, and thus, the current in the $V_b > 0$ range is modulated. It should be noted that the dominant mechanism for current modulation in this device is the change of the carrier injection barrier by the gate bias, not the change of the pentacene channel conductivity. The result of *I-V-T* measurement is consistent with the high ON/OFF ratio at low temperature in Figure 2(d) because this ratio is proportional to the exponential of $\Delta\phi_S/k_BT$, where $\Delta\phi_S$ is the energy barrier height variation in the given gate bias range. Moreover, note that the gradient of the energy barrier height was the largest around zero gate bias. This result implies that the Dirac point of graphene with the lowest density of states (DOS) existed near Vg = 0 V. The gradient tended to decrease as the gate bias increased because the more carrier density was induced, resulting in more DOS in the graphene. Note that Ojeda-Aristizabal et al. also previously observed ϕ_S modulation of ~300 meV in a similar pentacene barristor structure[18].

In our study, I observed ϕ_S modulation of ~100 meV (difference of 220 and 320 meV). This difference may be related to the different quality of graphene used. Unlike pristine graphene obtained using the mechanical exfoliation method, the graphene used in this study, which was synthesized using chemical vapor deposition, may have more defect sources, such as grain boundaries, wrinkles, or PMMA residues[29–31], inducing unintended interface states at the graphene/pentacene junction. This may weaken the Fermi level unpinning of pentacene and disturb the energy barrier modulation.

In contrast to the apparent current modulation in positive V_b range, it is extremely limited in negative V_b range due to the negligible change of the barrier height at the interface between Au electrode and pentacene layer. The numerous DOS of Au contrary to graphene can be one of origins of this behavior. The weakened field by the induced carrier density in the graphene electrode can be another reason.

I observed that the energy barrier height variation ($\Delta\phi_S$) in the given gate bias range monotonically decreased as the bias voltage increased. Figure 2.6 presents the Arrhenius plots and corresponding barrier height (ϕ_s) modulation by the gate field (a) at $V_b = \pm 5$ V, (b) at $V_b = \pm 7$ V, and at (c) $V_b = \pm 10$ V. The barrier height was modulated more effectively at the positive bias voltage, but the rate of barrier height change ($\Delta\phi_s$) decreased as the bias increased (see Figure 2.7). This result implies that for the high bias voltage region another conduction mechanism rather than the thermionic emission is involved in the charge transport; that is the Poole-Frenkel (PF) model which will be described later.

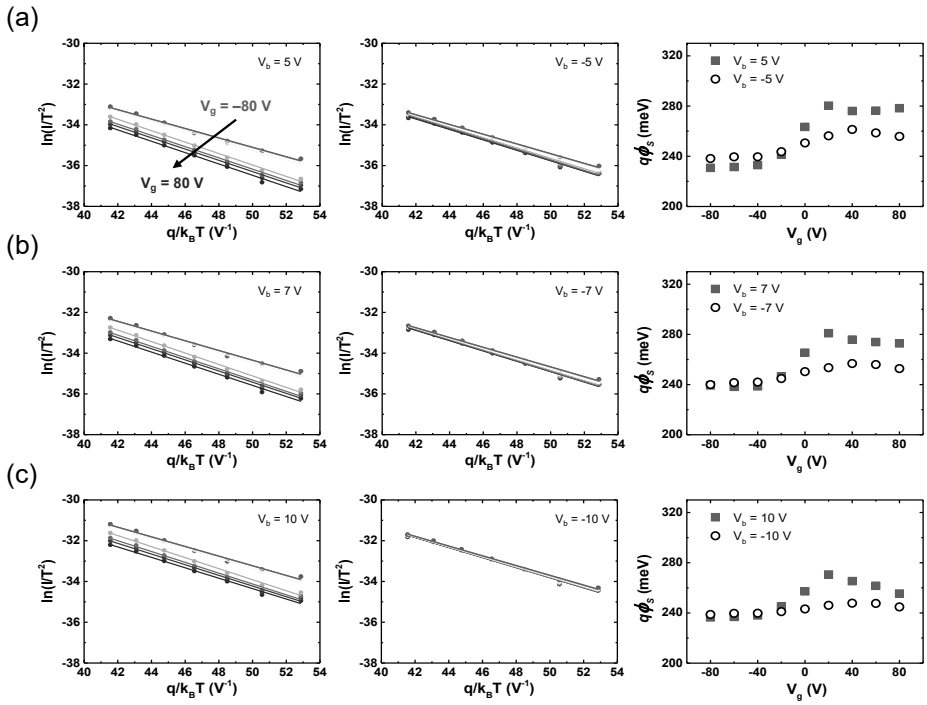

Figure 2.6 The Arrhenius plots and the corresponding Schottky barrier modulation (a) at $V_b = \pm 5$ V, (b) at $V_b = \pm 7$ V (b), and (c) at $V_b = \pm 10$ V in the gate bias voltage of –80 V < V_g < 80 V.

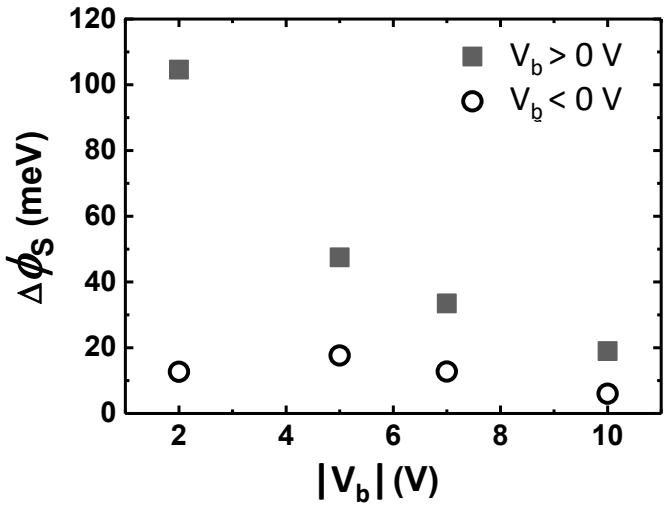

Figure 2.7 The Schottky barrier height variation ($\Delta\phi_s$) versus the bias voltage (V_b) in the gate bias voltage range of –80 V < V_g < 80 V where $\Delta\phi_s$ is defined as the difference between $\phi_s(V_g$ = +80 V) and $\phi_s(V_g$ = –80 V), which are extracted from Fig. 3b in the main text and the right parts of Fig. S2. Red squares and black circles correspond to the range of $V_b > 0$ and $V_b < 0$, respectively.

This result indicates that the contribution of the gate field to the current modulation decreased as the bias voltage increased, and it also suggests that another charge transport channel rather than thermionic emission occurred at high V_b range, which will be further explained later.

The schematic energy band diagrams of the pentacene barristor that can explain the above results are presented in Figure 2.5(c) and (d). When a positive voltage is applied to the graphene electrode, the hole carriers flow from graphene into the junction, passing through the energy barrier at the graphene/pentacene contact

(Figure 2.5(c)). In this case, the I_b-V_b relation is approximated using Eq. 2.1, where ϕ_S is the Schottky barrier height in the graphene/pentacene interface. The gate field effectively tunes this injection barrier because the Fermi level of pentacene is not pinned to the Fermi level of graphene due to its low density of states and small number of electrons near the Dirac point. Under the positive V_b condition, the negative gate bias voltage elevates the energy bands of both graphene and pentacene. Therefore, hole-rich graphene and the reduced barrier lead to the large current flow. When a positive gate bias is applied, the charge transport is restrained due to the increased energy barrier at the graphene/pentacene contact. In contrast, if a negative V_b is applied, then the hole carriers flow from the Au top electrode to the pentacene layer, and thus, the Schottky barrier in the Au/pentacene interface (ϕ_{Au}) is involved in the charge transport (Figure 2.5(b)). In this case, the Fermi level of pentacene pinned to the Fermi level of Au, and the corresponding energy barrier heights are hardly changed by the unscreened gate electric field penetrating the graphene/pentacene layer. Therefore, the current at the negative V_b range remains almost constant while the gate bias is changed.

2.3.3. Bias-dependent current modulation

To understand the $\Delta\phi_S$ dependence on bias, I investigated another type of charge transport through this heterojunction, namely, the Poole-Frenkel (PF) model, which describes the conductance in materials with localized trap sites by a charge trapping/de-trapping process[32,33]. As shown in the upper part of Figure 2.8(a), if there are trap sites in the interface or bulk, then holes can be captured in the potential

well with a depth of ϕ_{PF} when zero field is applied through the junction, and this potential well depth is reduced by an electric field. As the finite electric field is applied, holes tunnel from the electrode to the localized states. Then, holes with sufficient thermal activation energy are able to transport along the valence band by escaping the potential well. The PF model also illustrates how the electric field applied in material reduces the potential well of trap sites as the following equation

$$I_b \propto F\exp\left(-\frac{\phi_{PF} - e\sqrt{eF/\pi\epsilon}}{kT}\right) \qquad \text{Eq. 2.2}$$

where E is the applied electric field within the trap site that reduces the effective barrier height for charge carriers to move into the valence band and ϵ is the permittivity of the material. The effective barrier height (ϕ_{eff}) described in the lower part of Figure 2.8(a) is the potential well height reduced by the finite field, *i.e.,* $\phi_{\mathrm{eff}} = \phi_{\mathrm{PF}} - q\sqrt{qE/(\pi\epsilon)}$. If the charge transport of our device follows the PF model, then the $\ln(I_b/V_b)$ versus V_b curves would show the linearity because E is given as V_b/d_p, where d_p is the thickness of pentacene (500 nm). Figure 2.8(b) presents the $\ln(I_b/V_b)$ versus V_b plots of the pentacene barristor at various gate biases. These curves show the linear relation only in the high bias voltage range ($V_b > 3$ V), which means that the PF model can be applied to the device in the high field region. However, this plot shows a non-linear trend when a low bias voltage ($V_b < 3$ V) is applied. This deviation from linearity implies that thermionic emission becomes more important as the bias is lowered. I note that the gate field also contributes to this deviation because the starting points of 'tails' (part deviating from the trend lines) and their deviations are dependent on V_g. This is reasonable because the charges are

injected to pentacene over the Schottky barrier modulated by the gate field in the thermionic emission model, which is the dominant transport mechanism in the low bias range. The effective barrier height (ϕ_{eff}) within the pentacene-graphene interface in a finite electric field can be extracted from the *I-V-T* measurement as the slope of the ln(I_b/E) versus $\sqrt{E}$ plot. Here, I consider the field induced by V_g and V_b as $E = V_b/\mathrm{d_p} + V_g/d_{ox}$, where d_p and $\mathrm{d_{ox}}$ are the thicknesses of the pentacene layer (500 nm) and SiO_2 (270 nm), respectively, and the portion of the gate field weakly screened by induced charge on the graphene sheet is neglected in this calculation. The result is illustrated in Figure 2.8(c). It is clear that the gate field dependence of ϕ_{eff} is stronger at low bias (V_b = 2 V) than at high bias (V_b = 10 V). This result supports the inference that the PF model is an important charge transport mechanism in our device structure. Because the gate field occupies a significant portion of the field within the graphene-pentacene interface when a low bias is applied, ϕ_{eff} is effectively modulated by the gate bias voltage, while ϕ_{eff} only shows a very small change at high V_b, where the gate field is negligible compared to the field induced by the bias voltage. The low ON/OFF ratio in the high V_b region can also be explained in this context; because the field induced by the bias voltage contributes to barrier height modulation considerably more than the gate field, the current cannot vary effectively. I also observed that the slopes of the trend lines for the high-temperature range (T > 280 K) in the Arrhenius plots are hardly affected by the gate bias(Figure 2.6), which is further support for the PF model[32,34].

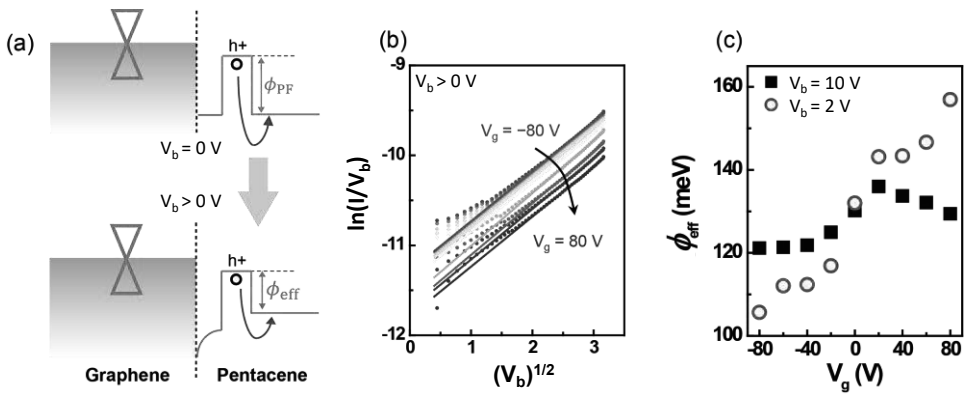

Figure 2.8 (a) The band diagram corresponding to the Poole-Frenkel model (upper) when zero field and (lower) a finite field is applied. The hole injects to trap sites and transports through the valence band of pentacene. (b) Plot of $\ln(I_b/V_b)$ versus V_b in various V_g in which the Poole-Frenkel conduction is featured as linear fitting in the high V_b range. (c) The modulation of effective barrier height (ϕ_{eff}) of trap sites in non-zero field situation by gate bias voltage at $V_b = 2$ V (red circles) and at $V_b = 10$ V (black squares).

2.4. Conclusion

In summary, I fabricated and characterized graphene/pentacene/Au vertical hetero-structure. These devices have unique electrical properties compared to conventional (planar) pentacene thin film transistors. The current-voltage curves were non-linear and asymmetric, and they showed larger current flow in the positive bias voltage range. The current modulation induced by the gate field was also asymmetric. I conducted variable-temperature measurements and demonstrated that these electrical characteristics originated from the different energy barrier properties

at the graphene-pentacene and pentacene-Au contacts. The charge transport within this heterojunction is attributed to thermionic emission and the Poole-Frenkel model, which is consistent with the results of a previous study [18, 33]. The contribution of each transport model was dependent on the applied bias; As the bias increased, the dominant conduction channel changed from the thermionic emission to Poole-Frenkel conduction. At the same time, the hole injection barrier modulation became insensitive to the gate field, which resulted in low ON/OFF ratio in the high bias range. Since the thickness of the pentacene layer may also affect the current between the electrodes, further investigations in terms of variable thickness of the pentacene would be desirable. This research on the electrical properties of organic heterostructure based on graphene can be exploited in various organic devices, including rectifiers, light-emitting diodes, memory, and other multi-functional electrical components.

References

[1] Novoselov K S, Geim A K, Morozov S V, Jiang D, Katsnelson M I, Grigorieva I V, Dubonos S V and Firsov A A 2005 *Nature* **438** 197

[2] Barone V, Hod O and Scuseria G E 2006 *Nano Lett.* **6** 2748

[3] Geim A K and Novoselov K S 2007 *Nat. Mater.* **6** 183

[4] Wassmann T, Seitsonen A P, Saitta A M, Lazzeri M and Mauri F 2008 *Phys. Rev. Lett.* **101** 096402

[5] Geim A K 2009 *Science* **324** 1530

[6] Wu Z S, Ren W, Gao L, Zhao J, Chen Z, Liu B, Tang D, Yu B, Jiang C and Cheng H M 2009 *ACS Nano* **3** 411

[7] Liu W, Jackson B L, Zhu J, Miao C Q, Chung C H, Park Y J, Sun K, Woo J and Xie Y H 2010 *ACS Nano* **4** 3927

[8] Lee S, Jo G, Kang S J, Wang G, Choe M, Park W, Kim D Y, Kahng Y H and Lee T 2011 *Adv. Mater.* **23** 100

[9] Lee W H, Park J, Sim S H, Jo S B, Kim K S, Hong B H and Cho K 2011 *Adv. Mater.* **23** 1752

[10] Jo G *et al.* 2010 *Nanotechnology* **21** 175201

[11] Han T H, Lee Y, Choi M R, Woo S H, Bae S H, Hong B H, Ahn J H and Lee T W 2012 *Nat. Photonics* **6** 105

[12] Wang X, Zhi L and Mullen K 2008 *Nano Lett.* **8** 323

[13] Miao X, Tongay S, Petterson M K, Berke K, Rinzler A G, Appleton B R and Hebard A F 2012 *Nano Lett.* **12** 2745

[14] Yang H, Heo J, Park S, Song H J, Seo D H, Byun K E, Kim P, Yoo I, Chung H J and Kim K 2012 *Science* **336** 1140

[15] Georgiou T *et al.* 2013 *Nat. Nanotechnol.* **8** 100

[16] Yu W J, Li Z, Zhou H, Chen Y, Wang Y, Huang Y and Duan X 2013 *Nat. Mater.* **12** 246

[17] Liu Y, Zhou H, Cheng R, Yu W, Huang Y and Duan X 2014 *Nano Lett.* **14** 1413

[18] Ojeda-Aristizabal C, Bao W and Fuhrer M S 2013 *Phys. Rev. B* **88** 035435

[19] Liu Y, Zhou H L, Weiss N O, Huang Y and Duan X F 2015 *ACS Nano* **9** 11102

[20] Oh G, Kim J S, Jeon J H, Won E, Son J W, Lee D H, Kim C K, Jang J, Lee T and Park B H 2015 *ACS Nano* **9** 7515

[21] Shih C J, Pfattner R, Chiu Y C, Liu N, Lei T, Kong D S, Kim Y, Chou H H, Bae W G and Bao Z N 2015 *Nano Lett.* **15** 7587

[22] Lee W H, Park J, Sim S H, Lim S, Kim K S, Hong B H and Cho K 2011 *J. Am. Chem. Soc.* **133** 4447

[23] Ishii H, Sugiyama K, Ito E and Seki K 1999 *Adv. Mater.* **11** 605

[24] Lee C G, Park S, Ruoff R S and Dodabalapur A 2009 *Appl. Phys. Lett.* **95** 023304

[25] Amy F, Chan C and Kahn A 2005 *Org. Electron.* **6** 85

[26] Diao L, Frisbie C D, Schroepfer D D and Ruden P P 2007 *J. Appl. Phys.* **101** 014510

[27] Sze S M, Coleman D J and Loya A 1971 *Solid-State Electronics* **14** 1209

[28] Baccaran.G, Calzolar.Pu and Graffi S 1974 *J. Appl. Phys.* **45** 341

[29] Li X, Zhu Y, Cai W, Borysiak M, Han B, Chen D, Piner R D, Colombo L and Ruoff R S 2009 *Nano Lett.* **9** 4359

[30] Liang X *et al.* 2011 *ACS Nano* **5** 9144

[31] Wang D Y *et al.* 2013 *Adv. Mater.* **25** 4521

[32] Mitrofanov O and Manfra M 2004 *J. Appl. Phys.* **95** 6414

[33] Berke K, Tongay S, McCarthy M A, Rinzler A G, Appleton B R and Hebard A F 2012 *J. Phys. Condens. Matter* **24** 255802

[34] Sze S M 1967 *J. Appl. Phys.* **38** 2951

Chapter 3. Electrical Characteristics of Molecular Junctions Fabricated by Inverted Self-Assembled Monolayer Method

3.1. Introduction

The molecular electronics is a research field that studies fabrication and characterization of molecular junctions consisting of single-molecules or molecular assembly sandwiched by two electrical leads. By the number of molecules participating the electronic conduction, the molecular junctions are classified as the single (a few) molecular junctions[1–5], or molecular ensemble junctions[6–10]. Major structure for molecular ensemble junctions is a vertical stack of bottom electrode – molecular layer – top electrode and the self-assembly is a widely used method to form the molecular layer on the surface of bottom electrode by utilizing the self-bonding nature of particular moiety of the molecules.

Directly depositing another metal film, however, can damage the self-assembled monolayer (SAM) and make the most molecular junction electrically shorted[11]. Therefore, several methods such as inserting interlayer (for example. conducting polymer[12,13] or multi-layer graphene[14–16]) or transferring the top electrode already formed[17] have been introduced to increase the yield of molecular junctions. By these fabrication methods,

high-yield molecular junctions were achieved but there still exists limitation in

materials for bottom electrodes. For example, thiolates can be self-assembled on only a few kinds of metal such as gold or silver[18,19].

In this study, I suggest an inverted self-assembled monolayer (iSAM) method to overcome such limitation. The alkyl thiolate SAM is formed on the top electrode and this stack is transferred to the pre-made via-hole structure[13-17] (the structure in which bottom electrode is exposed through a hole by etching the insulating layer). I demonstrate that the current density of molecular junctions and junction yield are comparable to the previous research results. This method enables the materials such as graphene or indium tin oxide (ITO) to be adapted for the bottom electrode in molecular junctions.

3.2. Experiments

3.2.1. Device fabrication process

Figures 3.1(a)–(d) illustrate the fabrication process of iSAM molecular devices. This process is divided into the fabrication of upper part and lower part of the device. For making the upper part, gold top electrodes (Au^{TOP} 30 nm thick) were deposited on *p*-type (100) Si substrate with 270 nm thick SiO_2 surface by e-beam evaporation with shadow masks. Then, poly(methyl methacrylate) (PMMA) (5 % in anisole) was spin-coated (4000 rpm, 60 sec) and annealed at 200 ºC. To detach the PMMA/Au^{TOP} stack from the substrate, the sample was immersed in potassium hydroxide (KOH) solution (~25 %, 50 ºC) for 30 min (Figure 3.1(a)). As SiO_2 underneath PMMA or Au^{TOP} was etched by KOH, the PMMA/Au^{TOP} stack could be detached from the

substrate. This stack remained in the form of film without winkles or folding because of the support of the punched tape applied before the immersion. This film was rinsed several times with deionized water and dried in N_2 stream very carefully.

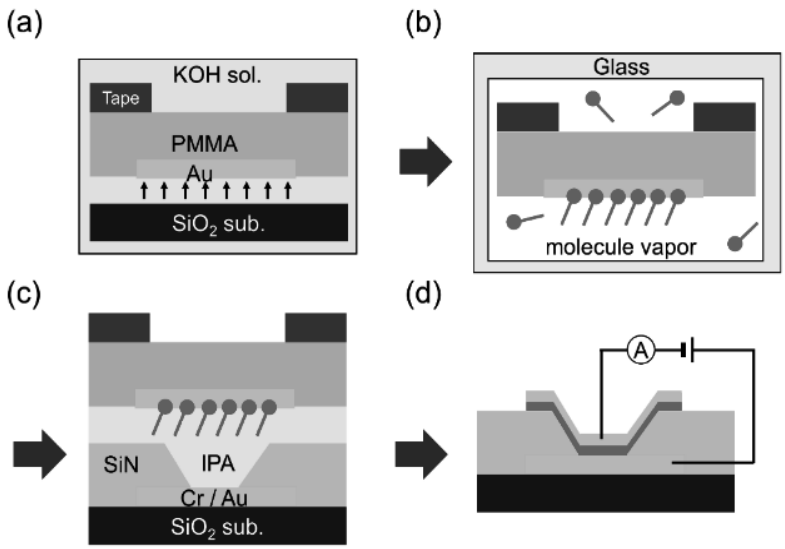

Figure 3.1 Fabrication processes of iSAM molecular junctions.

The molecules deposited on the Au^{TOP} were octanethiol ($CH_3(CH_2)_7SH$, denoted as C8) and dodecanethiol ($CH_3(CH_2)_{11}SH$, denoted as C12) (Figure 3.2(a)) widely used for benchmarking the molecular junctions. Since organic solvents such as ethanol or toluene deform or dissolve the thin PMMA film, the method immersing the sample into the molecular solution could not be applied to this study. Instead, I used vapor-phase deposition method[20] for formation of SAM on the Au^{TOP}. The PMMA/Au^{TOP} stack was moved into a vial in which a few drops of molecular liquid were included. While the sealed vial was on the hot plate (75 ºC, 4 hours) the molecules were evaporated and SAM was formed on the gold surface because of the chemical bonding between thiol moiety (-SH) and gold[19] (Figure 3.1(b)). SAM

deposition process was performed in the glove box of N_2 environment in which the O_2 and H_2O concentration were both under 1.0 ppm.

To fabricate the lower part of iSAM molecular junction, bottom electrode (Au^{BOT}) of Au 50 nm with Cr adhesive layer was made by sputtering and lift-off method. Then, 100 nm thick silicon nitride (SiN_x) was deposited by the plasma-enhanced chemical vapor deposition (PECVD) method and diameter 10 μm circular hole was created by photo-lithography and wet etching process. Au^{BOT} was exposed through this hole and remaining SiN_x blocked unintended current flow between Au^{TOP} and Au^{BOT}. Finally, the upper part and lower part of the junctions were aligned and attached (Figure 3.1(c)). A few drops of isopropanol (IPA) was added before transferring the PMMA/Au^{TOP} stack because the capillary action during vaporization of IPA facilitates the fine contact between two electrodes. The remaining PMMA film was removed by acetone. Figure 3.2(a) and (b) present the schematic illustration and optical microscopy image of the iSAM molecular device, respectively.

3.2.2. Device characterization

I measured the electrical characteristics of the iSAM devices with a semiconductor parameter analyzer (Keithley 4200 SCS) and a probe station (M5VC, MS tech) in room temperature and ambient condition. Bias voltage was applied to the Au^{BOT} while Au^{TOP} was grounded. The bias voltage was ranged from -1 V to 1 V. Since the surface roughness of electrode affects the formation of SAM and electric properties of molecular junction, I investigated the morphologies of both electrodes with atomic force microscopy (AFM) (NX-10, Park Systems). As described in AFM images

(Figure 3.2(c) and (d)), Au^{BOT} shows rougher surface than Au^{TOP}.

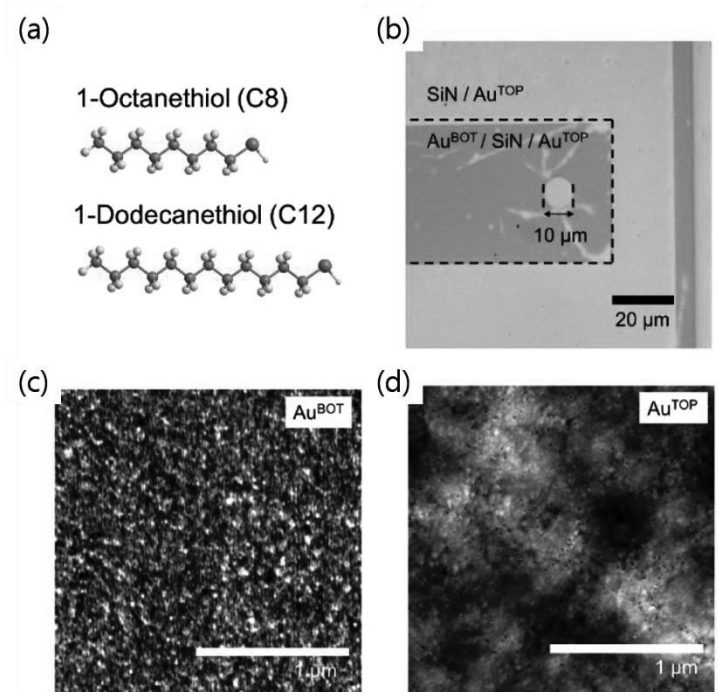

Figure 3.2 (a) Molecular structure of octanethiol (C8) and dodecanethiol (C12), (b) Optical image (top view) of molecular junction. Surface morphology (AFM images) of (c) bottom electrode and (d) top electrode.

3.3. Results and Discussions

To characterize the electric properties of iSAM molecular junctions with C8 and C12, I statistically analyzed the data obtained from the electric measurement. The detail information for the number of devices is summarized in Table 1. Total device yield (~29.6 %) is less than that of the result from the previous study based on the direct metal transferring method[17] due to the high fabrication failure rate (~37.0 %).

Molecules	Number of junctions	Fabrication failure	Working devices	Shorted	Open
C8	135	15	52	47	21
(%)	(100)	(11.1)	(38.5)	(34.8)	(15.6)
C12	135	85	28	5	17
(%)	(100)	(63.0)	(20.7)	(3.7)	(12.6)
Total	270	100	80	52	38
(%)	(100)	(37.0)	(29.6)	(19.2)	(14.1)

Table 3.1 The summary of the statistical analysis

There were two major fabrication failure cases; (i) In the step of SAM formation on Au^{TOP}, the PMMA film was slightly deformed by alkyl thiol molecules and several winkles remained in the Au^{TOP} film after finishing this step. Poor contact regions in the top electrode was made by these winkles and they were torn out when removing the PMMA. (ii) Even there was no winkle in the top electrode, Au^{TOP} films were often detached from the SiN_x surface due to their poor adhesion. The contact of Au^{TOP} to SiN_x surface was crucial to determine de device yield because 15 junctions shared one common top electrode.

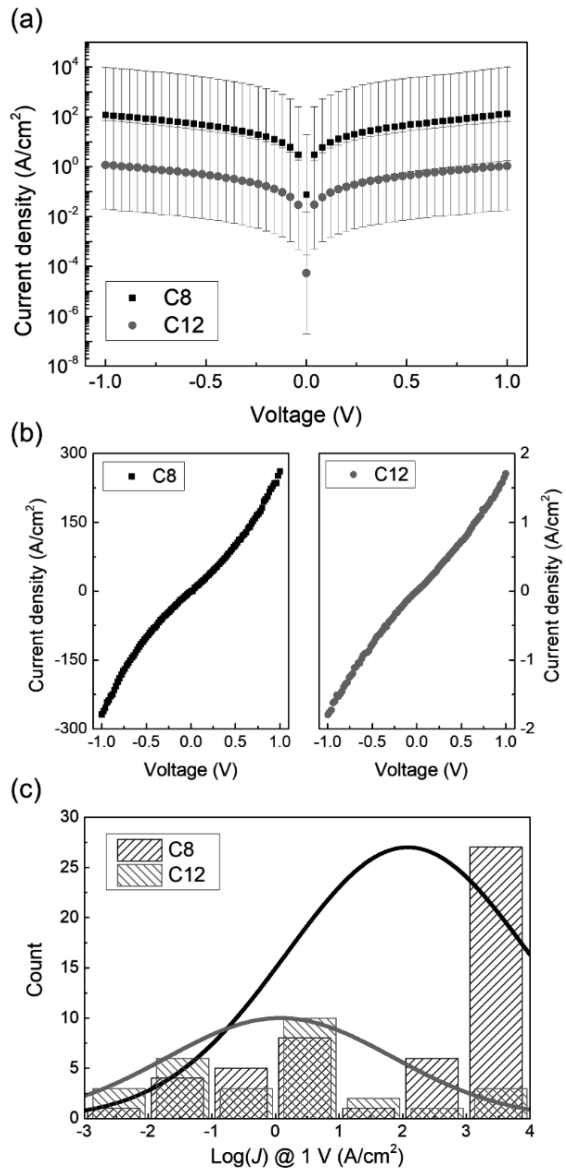

Figure 3.3 (a) Semi-log plot of statistical J – V data for C8 and C12 devices. (b) Typical non-linear J – V characteristics for molecular junction. (c) Histogram for the order of magnitude of the current density at 1 V for working devices.

Figure 3.3 presents the results from statistical analysis of the current density *versus* bias voltage (*J–V*) data of working molecular devices. As shown in the Figure 3.3(a), the mean current density of C8 devices is almost two orders of magnitude larger than that of C12 devices and the error bars express the standard deviation of the current density at each voltage step. Representative non-linear shapes of *J–V* graphs of C8 and C12 junctions are also shown in Figure 3.3(b). Figure 3.3(c) is a histogram of the current density in the order or magnitude at 1 V measured from working devices.

Although the mean values of current density for each type of the molecular junctions are in the range of the results reported previously, the large deviations were found. This broad distribution might originate from the defects on surfaces of each electrodes[21] or not uniform contacts between Au^{TOP} and Au^{BOT}. The surfaces of both electrodes consist of small grains, as shown in AFM images (Figure 3.2(c) and (d)). In other words, there are numerous grain boundaries which act as defects during formation of molecular layer. Mechanical defects were also induced when detaching and transferring the top electrode. Top electrodes with tiny winkles also broadened the distribution of current density. The gap caused by winkles in Au^{TOP} made uncertain contact area between two electrodes.

According to many studies in molecular electronics, off-resonant tunneling is known as the major conduction mechanism in the alkanethiolates junctions[22,23]. The current density decaying exponentially by the molecular length (i.e., $J = J_0 \exp(-\beta d)$ where β is the decay coefficient and d is molecular length) is an evidence that shows the current flows through the molecular wires in the junction. Figure 3.4 displays $\ln(J)$ *versus* the number of carbons in the molecules at given

bias voltage ranged from 0.2 V to 1.0 V in the step of 0.2 V. The value of β was obtained from the slope of linearly fitted lines at each bias voltages from Figure 3. I determined the average value of β as 1.17 per carbon or 0.92 $Å^{-1}$ (molecular length of C8 and C12 are 13.2 Å, 18.3 Å which are calculated from ChemDraw.). The β value obtained is in agreement with the results previously reported.

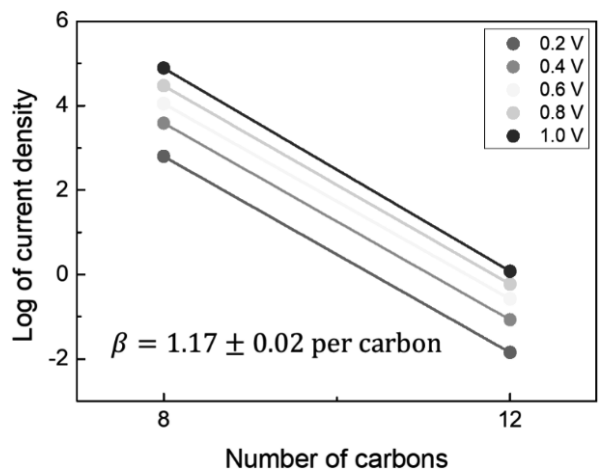

Figure 3.4 Plot of ln(J) as a function for the number of carbons at different bias voltages. The values of decay coefficient β (~1.17 per carbon) are extracted from the slopes of the exponentially fitted lines (solid lines).

3.4. Conclusion

In this study, I fabricated molecular devices with alkanethiolates using inverted self-assembly monolayer (iSAM) method and characterized their electrical properties. Molecular layer is self-assembled on the top electrode in contrast to the conventional molecular ensemble junctions made in the form of *via*-hole structure

with SAM deposited on the bottom electrodes. Electrical characteristics of iSAM devices including average current level and decay coefficient is consistent with the references but suppressing fabrication failure and controlling the defects in junctions are remaining challenges to improve device yield. In the platform of molecular junctions I investigated, alternative materials for bottom electrodes are adaptable. Therefore, I expect that functional molecular devices with various bottom electrode such as graphene or indium tin oxide can be developed by iSAM method.

References

[1] B. Xu, N. J. Tao, *Science* **2003**, *301*, 1221.

[2] M. Reed, C. Zhou, C. Muller, T. Burgin, J. Tour, *Science* **1997**, *278*, 252.

[3] J. Park, A. Pasupathy, J. Goldsmith, C. Chang, Y. Yaish, J. Petta, M. Rinkoski, J. Sethna, H. Abruña, P. McEuen, D. Ralph, *Nature* **2002**, *417*, 722.

[4] H. Song, Y. Kim, Y. Jang, H. Jeong, M. Reed, T. Lee, *Nature* **2009**, *462*, 1039.

[5] J. Xiang, B. Liu, S. Wu, B. Ren, F. Yang, B. Mao, Y. L. Chow, Z. Tian, *Angewandte Chemie Int Ed* **2005**, *44*, 1265.

[6] H. Haick, D. Cahen, *Accounts Chem Res* **2008**, *41*, 359.

[7] M. Chabinyc, X. Chen, R. Holmlin, H. Jacobs, H. Skulason, C. Frisbie, V. Mujica, M. Ratner, M. Rampi, G. Whitesides, *J Am Chem Soc* **2002**, *124*, 11730.

[8] M. Deshpande, M. Reed, J. Tour, *Appl Phys Lett* **1997**, *71*, 611.

[9] Y. Loo, D. Lang, J. Rogers, J. Hsu, *Nano Lett* **2003**, *3*, 913.

[10] J. Kushmerick, J. Naciri, J. Yang, R. Shashidhar, *Nano Lett* **2003**, *3*, 897.

[11] T.-W. Kim, G. Wang, H. Lee, T. Lee, *Nanotechnology* **2007**, *18*, 315204.

[12] H. B. Akkerman, P. W. M. Blom, D. M. de Leeuw, B. de Boer, *Nature* **2006**, *441*, 69.

[13] H. Jeong, D. Kim, G. Wang, S. Park, H. Lee, K. Cho, W. Hwang, M. Yoon, Y. H. Jang, H. Song, D. Xiang, T. Lee, *Adv Funct Mater* **2014**, *24*, 2472.

[14] G. Wang, Y. Kim, M. Choe, T. Kim, T. Lee, *Adv Mater* **2011**, *23*, 755.

[15] J. Koo, Y. Jang, L. Martin, D. Kim, H. Jeong, K. Kang, W. Lee, J. Kim, W.-T. Hwang, D. Xiang, E. Scheer, M. Kabdulov, T. Huhn, F. Pauly, T. Lee, *Acs Appl Mater Inter* **2019**, *11*, 11645.

[16] Y. Jang, H. Jeong, D. Kim, W.-T. Hwang, I. Jeong, H. Song, H. Jeong, M. Min, T. Lee, *J Nanosci Nanotechno* **2016**, *16*, 8565.

[17] H. Jeong, D. Kim, P. Kim, M. R. Cho, W.-T. Hwang, Y. Jang, K. Cho, M. Min, D. Xiang, Y. D. Park, H. Jeong, T. Lee, *Nanotechnology* **2015**, *26*, 025601.

[18] M. Schoenfisch, J. Pemberton, *J Am Chem Soc* **1998**, *120*, 4502.

[19] G. Poirier, E. Pylant, *Science* **1996**, *272*, 1145.

[20] S. Seong, H. Kang, S. Han, T. Sung, J. Park, T. Hayashi, M. Hara, J. Noh, *J Nanosci Nanotechno* **2017**, *17*, 5597.

[21] H. Jeong, W.-T. Hwang, P. Kim, D. Kim, Y. Jang, M. Min, D. Xiang, H. Song, Y. D. Park, H. Jeong, T. Lee, *Appl Phys Lett* **2015**, *106*, 063110.

[22] W. Wang, T. Lee, M. A. Reed, *Phys Rev B* **2002**, *68*, 035416.

[23] W. Wang, T. Lee, M. A. Reed, *J Phys Chem B* **2004**, *108*, 18398.

Chapter 4. Summary

In this thesis I described the results of the researches about the electrical properties of the organic molecular junctions modulated by the electric field and the development of a device fabrication method for large-area molecular junction in a solid-state platform.

In the first chapter, I briefly introduced the theoretical / experimental backgrounds of the molecular electronics. Several conduction mechanisms in the organic / molecular junction are reviewed. The Landauer formalism interprets the charge transport in the mesoscopic systems by the scattering approach, which describes the conductance as the transmission. Simmons model is another powerful but simple tool to illustrate the tunneling process through the insulating layer. The low / high voltage approximation of this model leads to the direct tunneling / field emission. Various testbeds for demonstrating the molecular devices were also introduced in two categories; Single-molecule junctions and Large-area junctions. Especially, large-area junctions built by transferring Au or Graphene electrodes were investigated in detail.

Gate-dependent electric characteristics in the pentacene barristor was depicted in the second chapter. This device is a vertical heterojunction of graphene / pentacene / Au on Si / SiO_2 substrate. These vertical heterojunctions exhibited distinct transport characteristics depending on the applied bias direction, which originates from different electrode contacts (graphene and gold contacts) to the pentacene layer. These asymmetric contacts cause a current rectification and current modulation

induced by the gate field-dependent bias direction. I observed a change in the charge injection barrier during variable-temperature current-voltage characterization, and we also observed that two distinct charge transport channels (thermionic emission and Poole-Frenkel effect) worked in the junctions, which was dependent on the bias magnitude.

In the next chapter, I demonstrated the molecular ensemble junctions fabricated by the inverted self-assembled monolayer (iSAM) method in which the molecular layer was deposited on the top electrode surface. The alkyl thiolate molecules were used to benchmark this method and I found that the electrical characteristics of these molecular junctions including the current level and the tunneling decay coefficient (β) were comparable to the results reported previously by conducting statistical analysis. I expect this iSAM method to enable the molecular junctions with bottom electrode of various materials including graphene.

Currently, the molecular rectifier whose rectification ratio is controlled by the gate voltage is under investigation with the results of the previous researches.

국문초록 (Abstract in Korean)

그래핀 전극 기반 수직구조 형태의 유기·분자 접합의 전기적 특성에 대한 연구

황왕택

서울대학교 물리천문학부

지난 수십년 간 분자 전자학은 분자와이어를 통한 전하 수송 현상을 이해하고 분자를 전기장치의 소자로써 활용하기 위하여 연구되어왔다. 저비용, 고집적, 기능성 분자의 합성, 그리고 자가조립이라는 분자전자학의 장점을 활용함으로써 저항이나 다이오드, 스위치, 메모리 또는 트랜지스터로써 작동하는 분자전자소자가 다양한 소자 플랫폼 상에서 구현되었다. 그러나 현대 논리회로를 구성하는 기본 요소인 전계효과 트랜지스터 (field-effect transistor, FET) 로서 작동하는 분자 소자에 대한 연구는 실제 응용에 제한이 있는 단일 분자 접합의 테스트 베드를 통해 주로 진행되었다. 이러한 점에서, 높은 소자 수율과 대량 생산의 이점을 활용할 수 있는 대면적 접합 플랫폼에서의 전계 효과 분자소자를 연구하고자 하였다.

첫번째 연구주제로서, 대표적 유기반도체 물질인 펜타센(pentacene)을 활용하여 배리스터(barristor) 소자를 제작하여 그 특성을 분석하였다. 이 소자는 전계 효과 분자접합과 그 구조나 전하 수송 원리가 유사하지만 더 용이한 방식으로 제작이 가능하다. 펜타센 배리스터의 전기적 특성을 관찰한 결과 인가한 bias 전압이나 gate 전압에 대하여 비대칭적인 양상을 보이는 것을 확인하였다. 또한 온도 변화에 따른 전기적 특성의 변화를 관측하였으며 이를 통해 bias 전압의 크기에 다라 thermionic

emission 이나 Poole-Frenkel conduction 이라는 두 가지 전도 원리에 따라 전하 수송이 발생한다는 것을 증명하였다.

그 다음 주제로서, 대면적 분자소자 제작의 대안적인 방식으로써 반전된 자가조립박막(self-assembled monolayer, SAM) 을 바탕으로 alkanethiol 분자접합을 제작하는 연구를 수행했다. SAM 이 하부 전극 상에 증착되는 일반적인 분자 앙상블 접합과 대조적으로, 이 소자에서는 미리 SAM 이 도포된 상부 전극을 하부 전극 위에 전사함으로써 접합을 형성한다. 대표적인 표준 분자인 alkanethiol 을 바탕으로 Au-molecule-Au 구조를 구현하였으며 앞선 연구들에서 다양한 방식으로 제작된 alkanethiol 분자접합들과 그 전기적 특성들을 비교하였다.

마지막으로, 위 연구 결과들을 바탕으로 게이트 전계에 의해 조절되는 분자정류소자가 연구 중에 있다. 다이오드와 같은 성질을 발현하기 위하여 ferrocenyl alkanethiol 분자가 활용되었고, 강한 전계 효과를 유도하기 위하여 top-gate 유전체로 이온젤 물질을 사용하였다. 이 소자의 정류 효과는 bias 전압과 gate 전압에 따라 변하는 것을 확인하였다.

Keywords: 분자 전자학, 그래핀, 자가조립 박막, 펜타센, 배리스터, 전하 수송, 알킬 사이올 분자

Student Number: 2013-20388